

Interseismic Deformation in the Gulf of Aqaba from GPS Measurements

Nicolás Castro-Perdomo^a, Renier Viltres^a, Frédéric Masson^b, Yann Klinger^c, Shaozhuo Liu^a, Maher Dhahry^e, Patrice Ulrich^b, Jean-Daniel Bernard^b, Rémi Matrau^a, Abdulaziz Alothman^d, Hani Zahran^e, Robert Reilinger^f, P. Martin Mai^a, Sigurjón Jónsson^{a,*}

^a*Physical Sciences and Engineering Division, King Abdullah University of Science and Technology (KAUST), Thuwal 23955, Saudi Arabia*

^b*IPGS, EOST Université de Strasbourg, CNRS, Strasbourg, France*

^c*Université de Paris, Institut de Physique du Globe de Paris, CNRS, F-75005 Paris, France*

^d*King Abdulaziz City for Science and Technology (KACST), Space Research Institute, Riyadh, Saudi Arabia*

^e*National Center for Earthquakes and Volcanoes, Saudi Geological Survey (SGS), Jeddah, Saudi Arabia*

^f*Department of Earth, Atmospheric, and Planetary Sciences. Massachusetts Institute of Technology. Cambridge, Massachusetts, USA*

Abstract

Although the Dead Sea Transform fault system has been extensively studied in the past, little has been known about the present-day kinematics of its southernmost portion that is offshore in the Gulf of Aqaba. Here we present a new GPS velocity field based on three surveys conducted between 2015 and 2019 at 30 campaign sites, complemented by 11 permanent stations operating near the gulf coast. Interseismic models of strain accumulation indicate a slip rate of $4.9^{+0.9}_{-0.6}$ mm/yr and a locking depth of $6.8^{+3.5}_{-3.1}$ km in the gulf's northern region. Our results further indicate an apparent reduction of the locking depth from the inland portion of the Dead Sea Transform towards its southern junction with the Red Sea rift. Our modelling results reveal a small systematic left-lateral residual motion that we postulate is caused by, at least in part, late postseismic transient motion from the 1995 $M_W 7.2$ Nuweiba earthquake. Estimates of the moment accumulation rate on the main faults in the gulf, other than the one

*Corresponding author

Email address: sigurjon.jonsson@kaust.edu.sa (Sigurjón Jónsson)

that ruptured in 1995, suggest that they might be near the end of their current interseismic period, implying elevated seismic hazard in the gulf area.

Keywords: Continental tectonics: strike-slip and transform, Space geodetic surveys, Neotectonics, Transient deformation, Plate motions

1. Introduction

The highest seismic hazard in Saudi Arabia and Egypt belongs to the areas bordering the Gulf of Aqaba (Fig. 1). This hazard is due to earthquakes on the offshore extension of the Dead Sea Transform (DST), a major fault system that accommodates left-lateral motion between the Arabian plate and the Sinai-Levant subplate (Freund et al., 1970; McKenzie, 1972). Several major earthquakes are known to have occurred along this southernmost portion of the DST during the last millennium, with the 1995 M_W 7.2 Nuweiba earthquake in the Gulf of Aqaba being the most recent one (Klinger et al., 1999; Holstetter, 2003). The decision by the Kingdom of Saudi Arabia to build a megacity in the NEOM area near the gulf has put this region under the spotlight, requiring further research efforts to improve the seismic hazard knowledge of the gulf area.

The DST formed as a result of the mid-Cenozoic breakup of the Arabo-African plate, and today it extends roughly 1000 km from the Red Sea rift to the East Anatolian fault (Garfunkel, 1981). The total estimated left-lateral offset of the DST south of the Dead Sea is about 105 km (e.g., Quennell 1958, 1959; Freund et al. 1970; McKenzie et al. 1970; Garfunkel 1981; Joffe and Garfunkel 1987) and the onset of its left-lateral strike-slip motion postdates 19-22 Ma (e.g., Bar et al. 1974; Steinitz et al. 1978; Bartov et al. 1980; Eyal et al. 1981; Joffe and Garfunkel 1987; Ben-Avraham et al. 2012; Nuriel et al. 2017). These estimates translate to an average slip rate between 4.8 mm/yr and 5.5 mm/yr since the initiation of fault motion along the southern part of the DST comprising the Jordan Valley and Wadi Arabah faults.

The geomorphology along the strike of the DST is marked by a series of pronounced depressions, 5-20 km wide, corresponding to pull-apart basins. These

morphological depressions form at jogs between discontinuous segments of the DST and are usually delimited by both normal and strike-slip faults (e.g., Garfunkel 1981; Ben-Avraham and Zoback 1992; Klinger et al. 1999; Ben-Avraham et al. 2012). From north to south, these depressions comprise the Ghab and Hula basins, the Sea of Galilee, the Dead Sea and the Gulf of Aqaba (see inset in Fig. 1). This series of pull-apart basins formed by left-lateral shear along left-stepping en échelon fault segments, which results in rhomb-shaped grabens subjected to left-lateral shear and extension (Quennell, 1959; Garfunkel, 1981). Despite being primarily a transtensional fault system (Garfunkel, 1981), a major ~200 km long restraining bend characterises the central part of the DST in Lebanon and Syria (e.g., Heimann and Ron 1987; Gomez et al. 2007). This segment deviates 20° - 30° from the main trend of the DST and accounts for ~1.6 mm/yr of convergent motion between the Sinai and Arabian plates at that latitude (e.g., Elias et al. 2007; Gomez et al. 2007).

Historical records, paleoseismic trenching and geomorphological studies indicate that many destructive earthquakes have occurred along the DST over the past two millennia (e.g., Ambraseys 2009; Agnon 2014; Meghraoui 2015; Klinger et al. 2015; Lefevre et al. 2018). Two successive earthquakes occurred in 363 AD, affecting more than 20 towns in Palestine and Syria (Ambraseys, 2009). According to Thomas et al. (2007), these earthquakes caused extensive destruction at several localities in southern Wadi Arabah. This observation is in agreement with Klinger et al. (2015), who reported an event horizon in a trench located 30 km north of the city of Aqaba (Jordan) that could be related to these earthquakes.

A major historical earthquake occurred in 1068 AD in the gulf area, destroying the town of Eilat (Ambraseys, 2009). Zilberman et al. (2005) reported that the earthquake was strong enough to rupture the surface along the Eilat fault, affecting an irrigation system. Historical records document another violent earthquake in 1212 AD. This earthquake was strongly felt in Eilat and caused damages to the monastery of St Catherine in the Sinai Peninsula (Ambraseys, 2009). This event was identified in a trench close to the village of Qatar in

southern Jordan (Klinger et al., 2015), and a brecciated layer associated with this earthquake was also reported by Kagan et al. (2011) in the Dead Sea basin. The last major historical earthquake reported in the gulf area occurred in 1588. Despite its location and magnitude are a subject of debate, intense shaking was documented as far as Cairo and Madinah, suggesting an epicentre in the northern Red Sea region (Ambraseys, 2009). Finally, the largest instrumental earthquake along the entire DST was the M_W 7.2 Nuweiba Earthquake, which struck the Gulf of Aqaba area on November 22, 1995, causing significant damage in nearby coastal communities in Egypt, Saudi Arabia, Jordan and Israel (Klinger et al., 1999; Hofstetter, 2003).

The gulf itself is about 180 km long and up to 25 km wide (Ben-Avraham et al., 1979; Garfunkel, 1981), and its structure is dominated by three left-stepping en échelon faults bounding a series of pull-apart basins (Ben-Avraham et al. 1979; Ben-Avraham 1985; Ribot et al. 2021, Fig. 1). The northernmost fault segment within the gulf is the Eilat fault. This fault is approximately 59 km long and constitutes the western boundary of the Eilat deep. The central fault segment is the Aragonese fault, which extends approximately 53 km, bounding the Eilat deep to the east and the Aragonese deep to the west. The Arnona fault constitutes the southernmost segment, extending roughly 83 km and forming the western boundary of the Dakar and Tiran deeps. Compelling evidence indicates that the Aragonese fault segment ruptured during the Nuweiba earthquake, while the other segments have not released significant seismic moment in the past several centuries (Shamir et al., 2003; Hofstetter, 2003; Baer et al., 2008; Ribot et al., 2021).

The seismic activity in the gulf is characterised by the occurrence of swarms, which have been observed since the deployment of the first regional seismic networks in the area (El-Isa et al. 1984; Alamri et al. 1991 as cited in Klinger et al. 1999). Significant swarm activity was reported in 1983, 1990 and 1993, reaching M_W 6.1 (El-Isa et al. 1984; Pinar and Türkelli 1997; Klinger et al. 1999, Fig. 2). Most earthquakes in the gulf exhibit predominantly left-lateral motion. However, some of them show significant normal motion, as evidenced

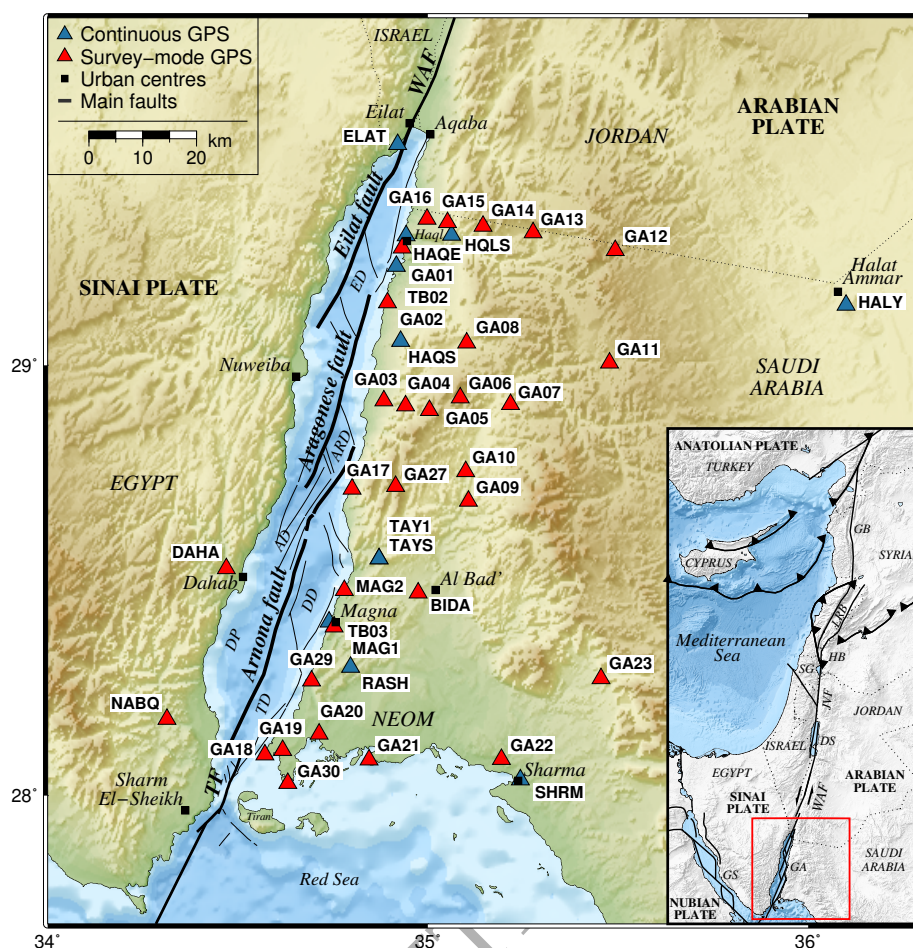


Figure 1: Mapped faults in the Gulf of Aqaba along with the GPS stations used in this study. Permanent and campaign GPS sites are shown as blue and red triangles, respectively. Fault traces and pull-apart basins are based on Ribot et al. (2021). The inset shows the area of interaction of the Arabian, Nubian, Sinai and Anatolian plates. Shaded topography is based on the SRTM30 PLUS digital elevation model (Becker et al., 2009) and regional-scale fault traces in the inset are compiled from Le Béon et al. (2008). TD, Tiran Deep; TF, Tiran Fault; DP, Dahab Plateau; DD, Dakar Deep; AD, Arnona Deep; ARD, Aragonese Deep; ED, Eilat Deep; GS, Gulf of Suez; GA, Gulf of Aqaba; WAF, Wadi Arabah Fault; DS, Dead Sea; JVF, Jordan Valley Fault; SG, Sea of Galilee; HB, Hula Basin; LRB, Lebanese Restraining Bend; GB, Ghab Basin.

by the pure normal slip reported for the largest event during the 1993 earthquake swarm (Klinger et al., 1999; Hofstetter, 2003). More recently, in June 2015, a M_W 5.2 strike-slip earthquake struck the gulf area, causing strong shaking in nearby communities and an aftershock sequence that lasted for more than two

weeks (El-Aal and Badreldin, 2016). Recent seismic data collected by the Saudi Geological Survey (SGS) show that earthquakes concentrate along, and are sub-parallel to the gulf fault system, as shown in Fig. 2.

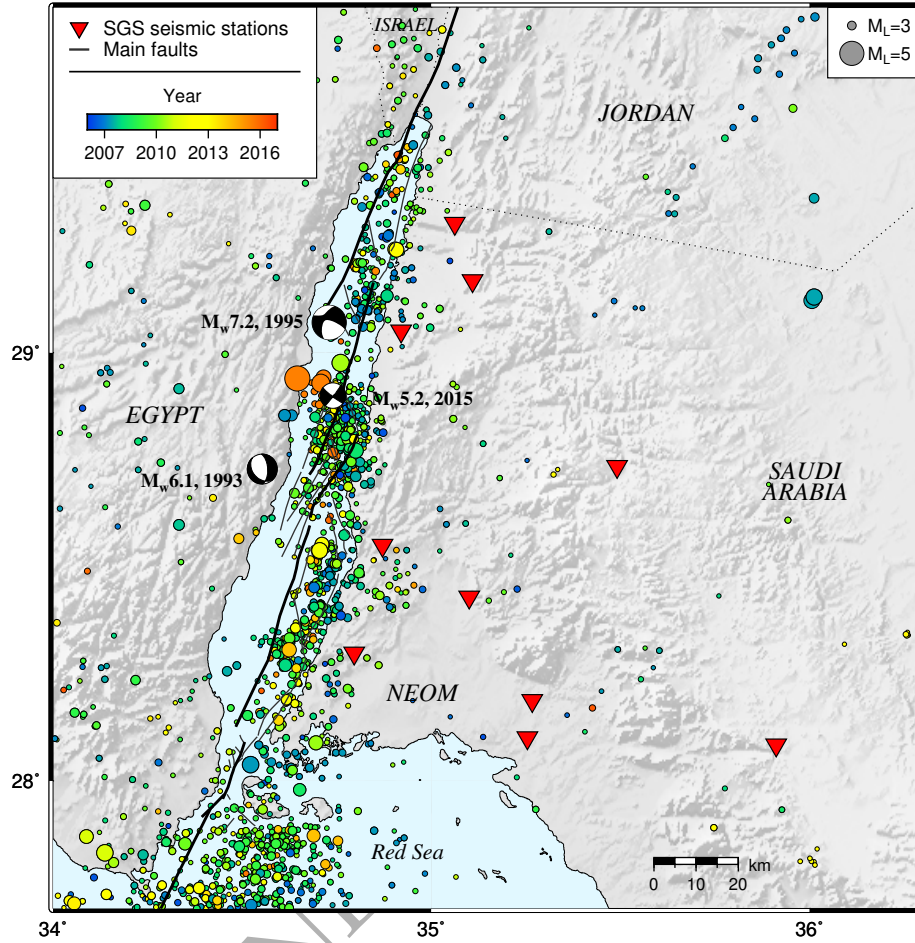


Figure 2: Earthquake locations ($M_L \geq 1.5$) in the Gulf of Aqaba region from January 2006 to March 2016 with circle sizes scaled according to earthquake magnitude and colours according to date. Focal mechanisms of the 1993 M_W 6.1, 1995 M_W 7.2 and 2015 M_W 5.2 earthquakes are from the National Earthquake Information Center (NEIC, <https://earthquake.usgs.gov>), the Global Centroid-Moment-Tensor (GCMT) catalog (Dziewonski et al., 1981; Ekström et al., 2012) and El-Aal and Badreldin (2016), respectively. Seismic stations operated by the Saudi Geological Survey (SGS) are shown as red inverted triangles. Note that the one-sided geometry of the SGS seismic network might bias epicentral locations.

The present-day crustal deformation along the DST north of the Gulf of Aqaba has been extensively analysed in terms of interseismic strain accumu-

lation (e.g., McClusky et al. 2003; Wdowinski et al. 2004; Gomez et al. 2007; Le Béon et al. 2008, 2010, 2012; Al Tarazi et al. 2011; Sadeh et al. 2012; Mahmoud et al. 2013; Masson et al. 2015; Hamiel et al. 2016, 2018a). However, only four GPS studies have provided slip rate estimates across the fault system in the gulf area. By implementing a back-slip model, Mahmoud et al. (2005) derived a slip rate of 4.4 ± 0.3 mm/yr, assuming a fixed locking depth of 13 km. A similar approach was followed by Reilinger et al. (2006), who reported a slip rate of 4.5 ± 0.3 mm/yr, holding the locking depth fixed to 12 km. ArRajehi et al. (2010) estimated slip rates of 4.8 ± 0.2 mm/yr in the gulf, and, more recently, Gomez et al. (2020) implemented a back-slip model and reported a slip rate of 4.9 ± 0.1 mm/yr. Unfortunately, these studies were unable to provide locking depth estimates due to the limited geodetic coverage near the gulf.

In this study, we use previously unpublished geodetic data to derive an updated crustal motion velocity field of the gulf. We further implement standard models of interseismic deformation to investigate the fault kinematics along the offshore segments of the DST fault system. Finally, we consider four possible model scenarios of time-dependent viscoelastic deformation produced by the Nuweiba earthquake and discuss whether postseismic transient motions are evidenced in the GPS data acquired near the gulf.

2. GPS Data and Analysis

A new survey-mode GPS network was installed in 2014 and surveyed three times in February 2015, March 2017 and May 2019 (see Tab. S1 and Fig. S1). This network consists of 27 GPS markers distributed over an area of 150 km by 70 km on the eastern gulf coast, extending from the Strait of Tiran in the south to the Jordan border in the north (Fig. 1). During the surveys, we also occupied three older markers installed by MIT near the municipalities of Al Bad' and Magna (sites BIDA, MAG1 and MAG2). These stations were measured annually between 2010 and 2014 (Gomez et al., 2020), and their data were reprocessed in our study. We also analysed the GPS data collected between 2000 and 2005

at the campaign sites DAHA and NABQ, which are located near the gulf coast on the Sinai Peninsula (McClusky et al., 2003; Mahmoud et al., 2005; Gomez et al., 2020).

To better understand the relative motion between the Sinai-Levant subplate and the Arabian plate, we processed data from 20 stations of the GIL network of continuous GPS monitoring in Israel (Wdowinski et al., 2001), covering a 19-year analysis period from 2000 to 2019 (see Fig. S2). Considering the rapid expansion of continuous GPS networks in Saudi Arabia, we incorporated data from additional 11 permanent stations near the gulf (HAQS, HQLS, TAY1, HAQE, SHRM, BEJD, TB02, TB03, HALY, RASH and TAYS). Our research significantly improves the GPS station coverage near the Gulf of Aqaba compared to previous studies, which relied on sparse GPS data in this area (e.g., McClusky et al. 2003; Mahmoud et al. 2005; Reilinger et al. 2006; ArRajehi et al. 2010; Gomez et al. 2020). Nevertheless, near-fault GPS observations are limited to distances greater than 8 km due to the presence of the gulf itself and the lack of offshore geodetic measurements.

We analysed the GPS data using the GAMIT/GLOBK software package version 10.70 (Herring et al., 2018) following a three-step approach described in detail by Dong et al. (1998). Daily carrier phase data from campaign and permanent stations were analysed separately to improve the processing efficiency (e.g., Bock et al. 1997). Following this strategy, we obtained two sets of loosely constrained solution vectors and covariance matrices. Both solutions share a set of 16 reference sites with well-determined coordinates and velocities, which we used to tie our final combined solution to the International Terrestrial Reference Frame (ITRF) 2014 (Altamimi et al., 2017). Campaign solutions were then merged with the continuous ones to get a final solution with ambiguities resolved and loose constraints on estimated parameters.

Combined solutions were used to estimate position time series and site velocities in GLOBK. The reference frame realisation was achieved by imposing tight constraints to the coordinates and velocities of 16 sites that comprise the reference network (ZIMM, GRAZ, ONSA, JOZE, WSRT, KIT3, IISC, POLV,

ARTU, POL2, MAS1, RABT, YEBE, DGAR, MBAR, NKLK), minimising in an iterative scheme their position adjustments with respect to their ITRF2014 a priori coordinates by estimating a six-parameter Helmert transformation. Finally, we accounted for time-correlated errors in the position time series by characterising their noise spectrum using the Hector software package version 1.7.2 (Bos et al., 2013). Since campaign stations do not have enough observations to estimate the time-correlated noise in their position time series, we used the mean random walk values obtained for the permanent stations in the study area ($4.5 \cdot 10^{-7} \text{ m}^2/\text{yr}$ and $1.5 \cdot 10^{-6} \text{ m}^2/\text{yr}$ for the horizontal and vertical velocity components, respectively). Following this approach, the resulting horizontal velocity uncertainties for stations within the new campaign GPS network deployed near the gulf vary between 0.5 and 1.0 mm/yr (see Tab.S2).

3. GPS Velocity Field

Time series and site velocities realised in ITRF2014 were rotated into stable Sinai reference frame. To perform this rotation, we estimated the Euler pole of the Sinai subplate with respect to ITRF2014 using five reliable stations located on the Sinai subplate at distances greater than 40 km from the DST (CSAR, ALON, YRCM, BSHM and RAMO), as shown in Fig. S2. The SINAI-ITRF2014 Euler pole derived here is $54.7 \pm 0.7^\circ \text{N}$, $347.8 \pm 4.0^\circ \text{E}$, $\omega = 0.417 \pm 0.021^\circ \text{Ma}^{-1}$, which is consistent with Euler vectors estimated in earlier studies (e.g., Wdowinski et al. 2004; Le Béon et al. 2008; Sadeh et al. 2012; Hamiel et al. 2016, 2018b,c; Hamiel and Piatibratova 2019). Observed GPS horizontal velocities for the sites on the Arabian plate show NNE motion relative to Sinai (Fig. 3), as reported in previous geodetic investigations (e.g., ArRajehi et al. 2010; Sadeh et al. 2012; Gomez et al. 2020). The velocity field thus reflects the left-lateral motion of the DST fault system. The increasing DST-parallel velocities towards the interior of the Arabian plate in this Sinai-fixed reference frame (Figs. 3 - 5a) suggest that the coastal areas bordering the gulf faults are currently undergoing interseismic strain accumulation.

Fig. 4 shows profiles of fault-parallel and fault-normal components of GPS-derived velocities relative to the Sinai-Levant subplate. These projections were performed assuming a single vertical fault with a strike of N16°E extending from the Strait of Tiran in the south to the northernmost tip of the gulf (dashed yellow line in Fig. 3). Increasing DST-parallel velocities towards the Arabian plate support active interseismic strain accumulation along the coastal areas adjacent to the gulf (Fig. 4a). We further note that the mean fault-normal velocity considering all the stations on the Arabian side of the gulf is $\sim 0.8 \text{ mm/yr}$ (Fig. 4b). This observation is consistent with a partly divergent motion between the Sinai and Arabian plates at this latitude, as suggested in previous investigations (e.g., Mahmoud et al. 2005; Reilinger et al. 2006; Gomez et al. 2020). However, the scatter observed in both velocity profiles suggests that the assumption of a single fault along the full extension of the gulf may be inadequate. This observation led us to consider different fault traces within the gulf based on the structural maps by Ben-Avraham (1985) and Ribot et al. (2021), see below.

4. Elastic Dislocation Model

We conducted an initial kinematic assessment of the GPS velocity field across the gulf by implementing a screw dislocation model (e.g., Weertman and Weertman 1964; Savage and Burford 1973). Following this approach, theoretical fault-parallel velocities v can be expressed as follows:

$$v = a + \frac{b}{\pi} \tan^{-1} \left(\frac{x}{D_L} \right) \quad (1)$$

where a defines the vertical origin of the arctangent curve, and x is the perpendicular distance measured from the fault trace. The fault is assumed to be locked during the interseismic period at depths extending from the surface down to a depth D_L (often referred to as locking depth), below which free slip occurs at a rate equivalent to the secular relative plate motion b . GPS measurements at distances within one-half the locking depth are required to accurately constrain fault locking depths, whereas far-fault observations are important to constrain

secular slip rates (Smith-Konter et al., 2011). This simple interseismic model has been extensively used to investigate kinematic parameters of many strike-slip and transform faults globally (e.g., Lisowski et al. 1991; Wright et al. 2001; Reilinger et al. 2006; Sadeh et al. 2012).

Here we analyse two velocity profiles across the Eilat fault in the north, and the Arnona and Tiran faults in the south, which include the largest number of

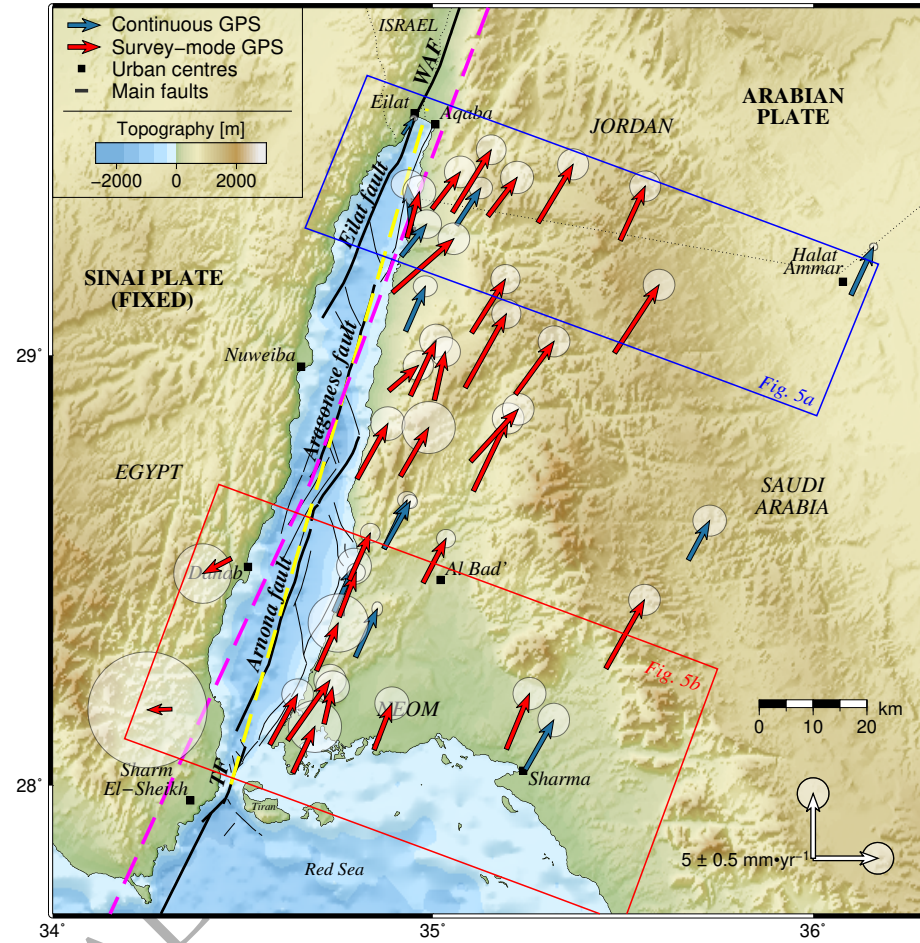


Figure 3: Horizontal GPS velocities relative to Sinai with 95% confidence ellipses. Permanent and campaign site velocity vectors are coloured in blue and red, respectively. The blue and red boxes indicate the location of the velocity profiles shown in Fig. 5a-b. The dashed yellow line corresponds to the assumed fault location used in Fig. 4a-b. The dashed magenta arc delineates the small circle around the Arabia-Sinai Euler pole derived in this study.

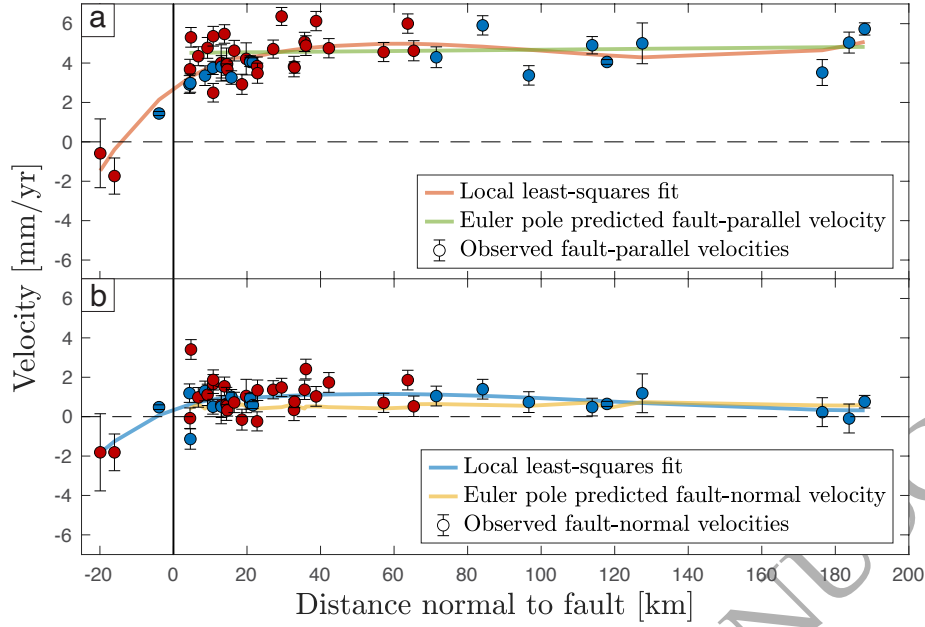


Figure 4: Profiles of a) fault-parallel and b) fault-normal velocities across Gulf of Aqaba assuming a single vertical fault striking N16°E along the gulf (dashed yellow line in Fig. 3). Site velocities are expressed in a Sinai-fixed reference frame, i.e., positive velocity values on the Arabian plate ($x > 0$) represent left-lateral motion in a) and opening in b) across the gulf. The solid orange and blue lines correspond to the best local least-squares fit to fault-parallel and fault-normal velocities, respectively. The least-squares fit was performed using a third-order Savitzky-Golay filter considering 39 data points per window. The pale green and yellow lines represent the fault-parallel and fault-normal velocities predicted by the Arabia-Sinai Euler Pole. Permanent and campaign site velocities are coloured in blue and red, respectively.

near-fault GPS stations. The northern profile extends from the city of Eilat at the northern tip of the gulf to the municipality of Halat Ammar, located 120 km inside the Arabian plate (Fig. 5a), assuming a fault strike of N22°E. The southern profile extends from Sharm El-Sheikh in the Sinai Peninsula to the city of Sharma in Saudi Arabia (Fig. 5b), and assumes a fault strike of N20°E. The sampling width of these profiles is based on the extension of the fault segments within the gulf, which overlap in certain areas forming pull-apart basins, as shown in Fig. 1. Following this criterion, the southern Eilat and the Aragonese pull-apart basins correspond to the limits of the northern and southern profiles, respectively. Unlike the northern and southern profiles, the central area across the Aragonese fault does not include enough near- and far-field GPS stations to

reliably constrain slip rates and locking depths. Moreover, there are no stations constraining GPS rates on the Sinai Peninsula west of the Aragonese fault. For these reasons, the central segment was not considered for slip-rate and locking depth inversions.

We constrained model parameters (i.e., a , b and D_L) and their uncertainties using a grid-search algorithm coupled with a Monte Carlo procedure that accounts for uncertainties in the fault position and stations' velocities. The best fit corresponds to the set of model parameters that results in the lowest root mean squared (RMS) error relative to the actual GPS observations (Fig. 5a-b). To estimate uncertainties in slip rates and locking depths, we conducted 10^4 Monte Carlo simulations, perturbing the location of the fault randomly within a range of ± 0.5 km and adding Gaussian noise to the GPS velocities within their 1-sigma uncertainties. In each Monte Carlo simulation, the grid-search explores the misfit (RMS) of the model for a range of values in the parameter domain, and selects the combination of model parameters that results in the lowest misfit. The strike (azimuth) of the fault segments was held fixed during the slip rate and locking depth inversions. However, we explored the effect of small perturbations (± 5 degrees) in fault strike on the final inversion results. We found that small variations in fault strike do not have a statistically significant impact on the slip rate and locking depth estimates, as shown in Fig. S3.

After performing the Monte Carlo inversion, we derived a 2×2 covariance matrix from the resulting distribution of slip rates and locking depths. From this covariance matrix, we estimated the width (ω) and height (h) of the confidence level ellipse, which are given by $\omega = 2 \times nstd \times \sqrt{\lambda_1}$ and $h = 2 \times nstd \times \sqrt{\lambda_2}$, where $nstd$ represents the desired confidence level (in standard deviations) and $\lambda_{1,2}$ are the eigenvalues of the covariance matrix. We followed this approach to derive 1-sigma (68%) confidence level ellipses, as shown in Fig. 5c-d.

Our results yielded a slip rate of $4.9^{+0.9}_{-0.6}$ mm/yr and a locking depth of $6.8^{+3.5}_{-3.1}$ km for the northern profile across the Eilat fault (red curve Fig. 5a). Further south, across the Arnona and Tiran faults, we derived a slip rate of $5.5^{+1.3}_{-0.9}$ mm/yr and a locking depth of $0.8^{+3.4}_{-0.8}$ km (red curve in Fig. 5b). Stations

GA12, GA13 and GA15 in the northern profile and GA19, GA20 and GA23 in the southern profile exhibit anomalous rates relative to nearby stations with no obvious explanation. These outliers could be related to local effects that may include unmodelled tropospheric signals, local deformation and seasonal loading, which are not modelled for the campaign stations. The inclusion of sites with anomalous behaviour in the slip rate and locking depth inversion is undesirable because they adversely affect fit to the data (e.g., [Sadeh et al. 2012](#)). For this reason, these stations were dismissed from the analysis, yielding the results given by the red curves in Fig. 5a-b.

To further analyse the effect of near-fault station rates on the final locking depth estimates, we considered additional scenarios omitting stations GA01 and GA16 in the northern profile and GA18 in the southern profile (blue curves in Fig. 5a-b). Our results show that the omission of sites GA01 and GA16 in the northern profile has a minor effect on the slip rate estimate but results in a deeper locking depth of 10.5 km. Similarly, excluding station GA18 in the southern profile results in a deeper locking depth estimate of 3.2 km compared with the 0.8 km obtained when including GA18 in the inversion. The 68% confidence level ellipses shown in Fig. 5c-d are elongated, showing a clear trade-off between slip rates and fault locking depths. As demonstrated in several studies, higher slip rates require deeper locking depths (e.g., [Wright et al. 2001](#); [Meade and Hager 2005](#); [Smith-Konter et al. 2011](#)). This correlation arises from the tight constraint on the near-field velocity gradient imposed by the dislocation model (see [Wright et al. 2001](#) for details).

Finally, we compared our results with the slip rates and locking depths derived by [Li et al. \(2021\)](#) based on the implementation of Sentinel 1 burst-overlap interferometry (BOI) in the lands bordering the gulf (light orange curves in Fig. 5a-b). Taken together, both results indicate shallower locking depths from north to south, towards the Red Sea rift. Our results further suggest that a very shallow locking depth or creeping is required in the southern part of the gulf to account for the low strain accumulation observed in this area. However, the current near-fault GPS data are insufficient to unambiguously discriminate

between shallow locking and full creep scenarios along the southern fault segments. These results motivated us to implement a more complex model of strain accumulation, which not only considers fault-parallel motions but also allows for tensile motions and rigid block rotations.

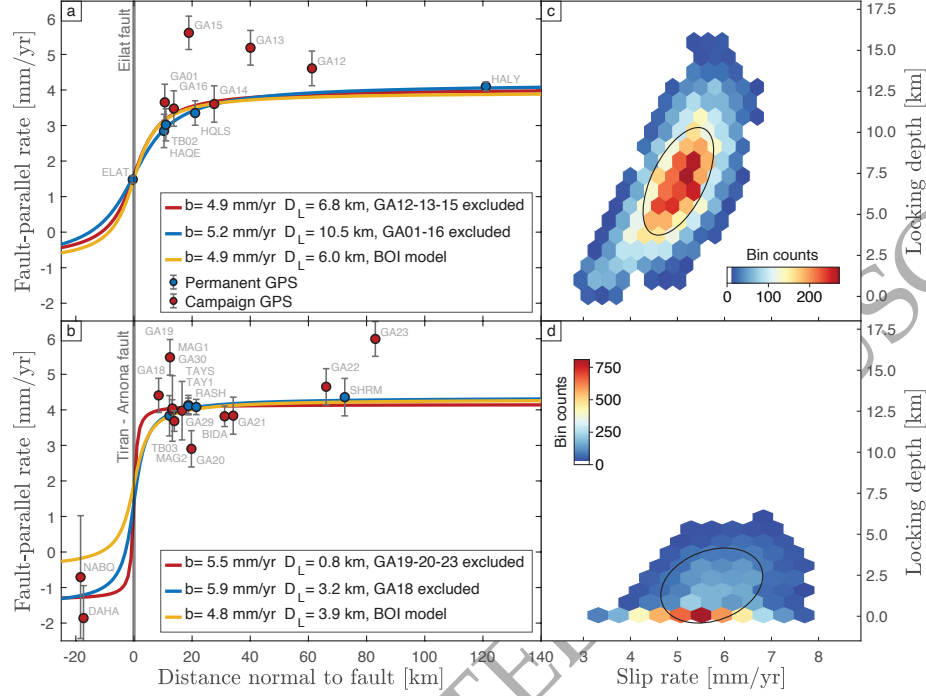


Figure 5: Observed fault-parallel velocities with 1-sigma uncertainties across the Eilat fault (panel a) and Tiran-Arnona faults (panel b) in comparison with predictions from elastic dislocation models in a Sinai-fixed reference frame. Panels c and d depict the results of the slip rate and locking depth inversions and 68% confidence level ellipses. The red curve in both profiles represents the global minimum considering a , b and D_L as free parameters. Results from Li et al. (2021), based on burst-overlap interferometric (BOI) observations, are shown in light orange.

5. Back-Slip Model

Interseismic deformation studies conducted further north along the DST in Israel, Jordan, Syria and Lebanon have shown that GPS-derived velocities can be well explained by rigid block movement bounded by a narrow deformation zone that accommodates the relative motion between them (e.g., Mahmoud et al.

2005; Reilinger et al. 2006; Gomez et al. 2007, 2020; Al Tarazi et al. 2011). This view is also supported by the distribution of instrumental and historical seismicity, which concentrates along the main fault strands of the DST fault system (Hofstetter et al., 2014). We thus next investigated whether the velocity field in the Gulf of Aqaba area can also be explained using a similar back-slip model.

We adopted the approach described by McCaffrey (2005, 2009) and defined two blocks representing the Sinai and Arabian plates. The boundary between them was modelled as a set of linear fault segments representing the main fault strands of the gulf mapped by Ben-Avraham (1985) and Ribot et al. (2021), with short relay faults connecting the segments (Figs. 6-7). Model-predicted velocities result from superimposing linear rates due to block rotations and those associated with the back-slip motion applied on block boundaries, which are estimated following Okada (1985).

The number of near-fault GPS observations is insufficient to reliably invert for the locking fraction distribution along the fault segments within the gulf, even for sparse discretisations of the fault planes. Hence, we considered three forward back-slip model scenarios defining the locking fraction of the fault segments a priori. In the first scenario, we imposed full interseismic locking on all the faults in the gulf (Fig. 6a). In the second scenario, we considered creep on the Arnona and Tiran faults (Fig. 6b). Finally, in the third scenario, we imposed creep on the Tiran fault only (Fig. 7). Locked faults were modelled as near vertical extending down to 7 km, based on our best-fit estimate across the Eilat fault. Creeping faults were modelled as free-slipping boundaries that do not produce any elastic strain. To evaluate the effect of implementing different fault geometries in our back-slip models, we ran an additional scenario assuming a dip angle of 65° for the Aragonese fault, as proposed by Baer et al. (2008). By comparing the resulting back-slip model residuals with those obtained assuming a vertical fault (Fig. 7), we show that the variance difference is not large enough to be statistically significant, as depicted in Fig. S5.

Considering that most stations in the gulf area have short time series (< 5

years), we did not optimise for rotation parameters during the back-slip modelling. Instead, we defined the Arabia-Sinai Euler pole a priori using the Sinai-ITRF2014 Euler vector derived in this study and the Arabia-ITRF2014 rotation pole reported by Altamimi et al. (2017). In this way, the back-slip applied on each locked fault in the gulf was determined by the Arabia-Sinai rotation pole (35.00°N , 8.78°E , $\omega=0.105^\circ\text{Ma}^{-1}$), assuming that no aseismic slip occurs during the interseismic period on those faults. Finally, we compared observed and back-slip predicted velocities in the gulf area and analysed the residual rates.

Our modelling results indicate that the coastal areas bordering the Arnona fault are undergoing strain accumulation. This is supported by the good fit to the data on the Arabian side of the gulf obtained by imposing full interseismic locking to the Arnona fault in the first model scenario (Fig. 6a) and the small but coherent southward residuals obtained in the second scenario, where creeping is assumed along the Arnona and Tiran faults (Fig. 6b). We analysed these residuals quantitatively, showing that when the Arnona fault is assumed to be fully locked, near-fault velocity residuals are close to zero (panels a and b in Fig. S6). In contrast, full-creep on the Arnona fault leads to a systematic bias of ~ 0.4 mm/yr and ~ 0.2 mm/yr in the North and East velocity components, respectively (panels c and d in Fig. S6). We also noted that the fit to the data across Tiran fault degrades if this fault is assumed to be locked during the interseismic period. This observation suggests that creeping might be required to explain the low interseismic strain accumulation observed across this fault. We found that the best fit to the data is obtained by implementing scenario 3, which considers full locking along all the fault segments except Tiran fault, which is modelled as a creeping fault. Scenario 3 explains the interseismic strain accumulation observed across the Arnona fault and the full-plate rate exhibited by near-fault GPS stations across Tiran fault (see Fig. 7a).

Our results further suggest a fault-parallel slip-rate of ~ 4.5 mm/yr and a tensile component of ~ 0.3 mm/yr along the main fault strands in the gulf, as determined from the relative plate motion (see Fig. 7a). The back-slip model succeeds in fitting 13 out of 17 GPS rates (76%) within their 95% confidence

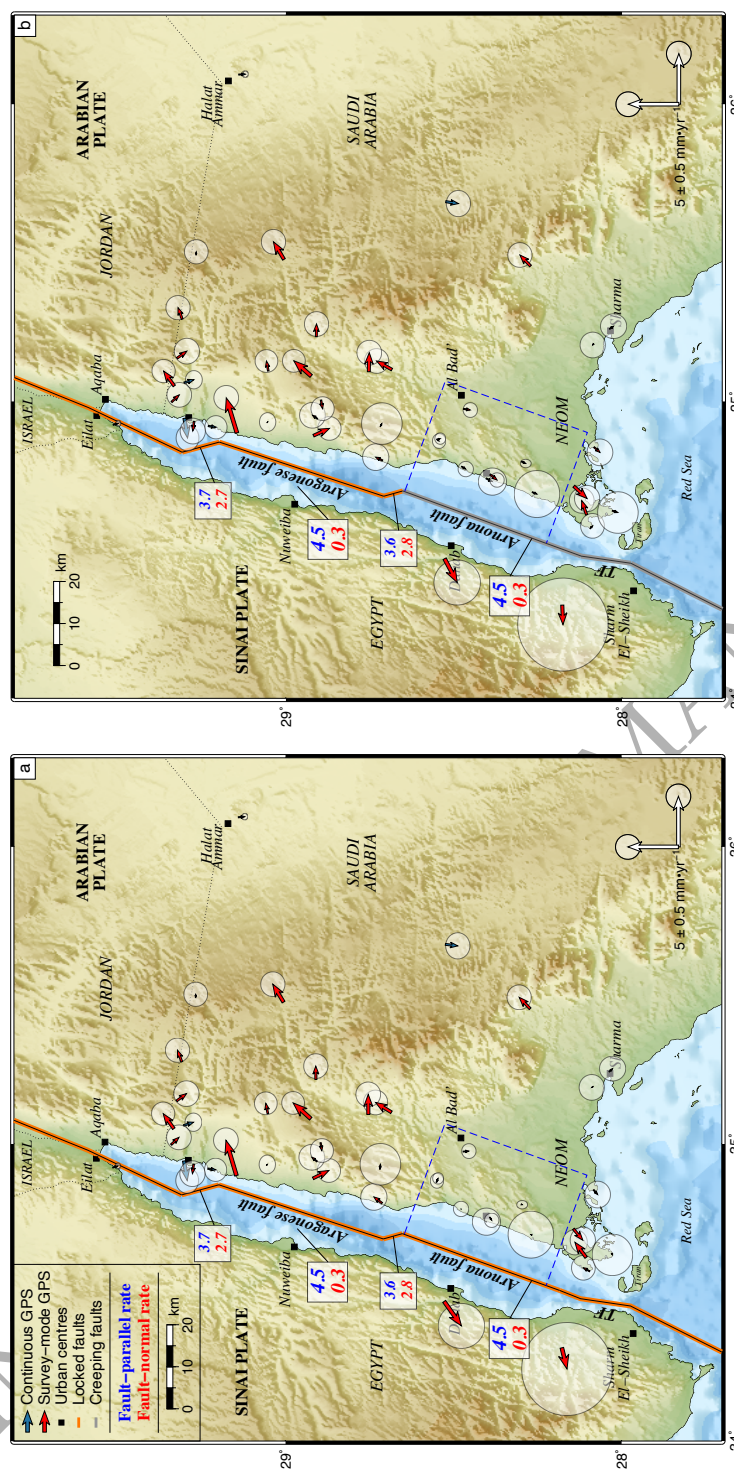
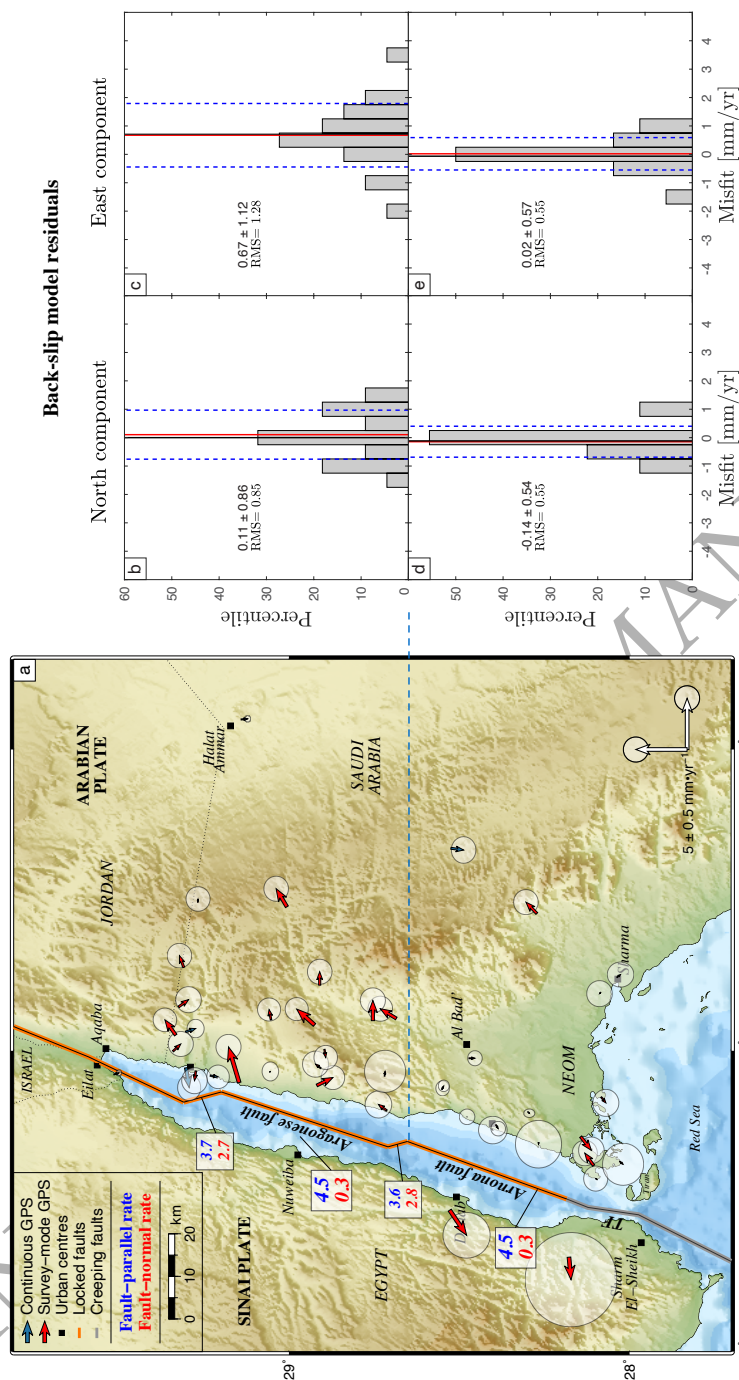


Figure 6: Panel a shows residual velocities after implementing the first back-slip model scenario assuming full interseismic locking on all the fault traces. Panel b shows the residuals obtained after implementing the second scenario assuming full creep along the Armona fault and the Tiran fault (TF). Orange and grey lines represent locked and creeping fault traces, respectively. Residual rates of seven near-fault stations within the blue dashed boxes are analysed in Fig. S6.



ellipses in the southern region of the gulf (east of the Arnona and Tiran fault traces). Nevertheless, our modelling results reveal an apparent reduction in the quality of the fit for most sites located in northern Gulf of Aqaba (east of the Aragonese fault trace), where only 12 out of 23 observations (52%) were fitted within their 95% confidence ellipses. Interestingly, residual velocities are not randomly distributed but are instead systematically directed towards the East-Northeast on the Arabian side of the gulf. This observation led us to investigate in more detail the nature of these residuals and their spatial distribution. For this purpose, we estimated descriptive statistics of the misfits, discriminating between stations in the northern and southern regions of the gulf.

The misfit distributions depicted in Fig. 7b-e quantitatively demonstrate that the magnitude of residual velocities differs between the northern and southern regions on the Arabian side of the gulf. Notably, the average magnitude of the east component of residual velocities in the northern area is about 0.7 mm/yr . This value contrasts with that observed east of the Arnona fault in the southern region of the gulf, where the east component of residual velocities is roughly zero. Similarly, but to a lesser extent, we observe a small discrepancy in the north component of residual velocities. The mean magnitude of the north component of residual velocities east of the Aragonese fault is 0.11 mm/yr , while the average value of the same velocity component observed east of the Arnona fault in the southern region of the gulf is -0.14 mm/yr . Our results thus suggest the existence of a left-lateral residual motion across the gulf that cannot be explained by block rotations and interseismic strain accumulation alone. These results drove us to study the potential influence of postseismic transient motions caused by the 1995, $M_w 7.2$ Nuweiba earthquake in the lands bordering the gulf.

6. Postseismic Modelling

Transient surface deformation has been systematically observed following large earthquakes spanning periods from months to decades (Scholz, 2002). Three time-dependent mechanisms are most often tested to explain such deformation

transients: Afterslip on and/or around the ruptured fault plane (e.g., [Savage et al. 1994](#); [Bürgmann et al. 1997](#)), poroelastic rebound (e.g., [Peltzer et al. 1996](#); [Jónsson et al. 2003](#)) and viscoelastic relaxation of the lower crust and upper mantle (e.g., [Pollitz 1997](#); [Freed and Bürgmann 2004](#)). The last one is the only process capable of producing postseismic deformation spanning both large spatial and long temporal scales ([Vergnolle et al. 2003](#) and references therein). Despite considerable efforts aimed at elucidating the underlying nature of the mechanisms controlling postseismic deformation, discriminating among them using geodetic measurements is challenging and is presently an active area of research (e.g., [Jónsson 2008](#); [Liu et al. 2020](#)).

Considering the limited GPS measurements in the years following the 1995 Nuweiba earthquake, the data are insufficient to invert for rheological parameters. Hence, we set up a series of forward models to analyse the postseismic surface deformation resulting from different lithospheric structures for the Gulf of Aqaba. For this purpose, we studied the viscoelastic relaxation following the methodology proposed by [Wang et al. \(2006\)](#) for a layered viscoelastic Earth model accounting for gravity effects. We used a simplified 1D velocity model of the gulf area from [Tang et al. \(2016\)](#) to define a layered Earth structure consisting of a Burgers viscoelastic half-space underlying a 30 km thick elastic layer, representing the Earth’s upper mantle and crust, respectively (see Fig. 8b-d). We also considered a three-layer Earth structure consisting of a 30 km elastic upper crust underlain by a biviscous lower crust and upper mantle (see Fig. 8e). The source of the $M_W 7.2$ Nuweiba earthquake was modelled using the distributed slip model derived by [Baer et al. \(2008\)](#) from ERS-1 and ERS-2 Interferometric Synthetic Aperture Radar (InSAR) data (see Fig. 9).

We explored four model scenarios by varying the transient and steady-state viscosities of the Burgers solids. In the first three scenarios, the viscosity of the underlying half-space was set based on the best-fit viscosity reported by [Piersanti et al. \(2001\)](#) for the Sinai-Suez area ($\sim 10^{18} \text{ Pa} \cdot \text{s}$). In the fourth scenario, we considered a thin crème brûlée rheological structure consisting of a 30 km elastic upper crust underlain by a biviscous lower crust and upper

mantle. Following the considerations above, in scenario 1, we assigned values of $1 \cdot 10^{18}$ and $1 \cdot 10^{19} \text{ Pa} \cdot \text{s}$ to the transient (η_K) and steady-state (η_M) viscosities, respectively. In scenario 2, we fixed η_K to $2 \cdot 10^{18} \text{ Pa} \cdot \text{s}$ and η_M to $2 \cdot 10^{19} \text{ Pa} \cdot \text{s}$. In scenario 3, we considered a higher transient viscosity of $1 \cdot 10^{19} \text{ Pa} \cdot \text{s}$ and a steady-state viscosity of $1 \cdot 10^{20} \text{ Pa} \cdot \text{s}$. Finally, in scenario 4, we defined steady-state viscosities of $2 \cdot 10^{18} \text{ Pa} \cdot \text{s}$ and $4 \cdot 10^{19} \text{ Pa} \cdot \text{s}$ for the lower crust and upper mantle, respectively (transient/steady-state viscosity = 0.1). We held fixed the ratio between effective and unrelaxed shear modulus (α) to a value of 0.5 in the first three scenarios, and 0.7 in the last model (see below).

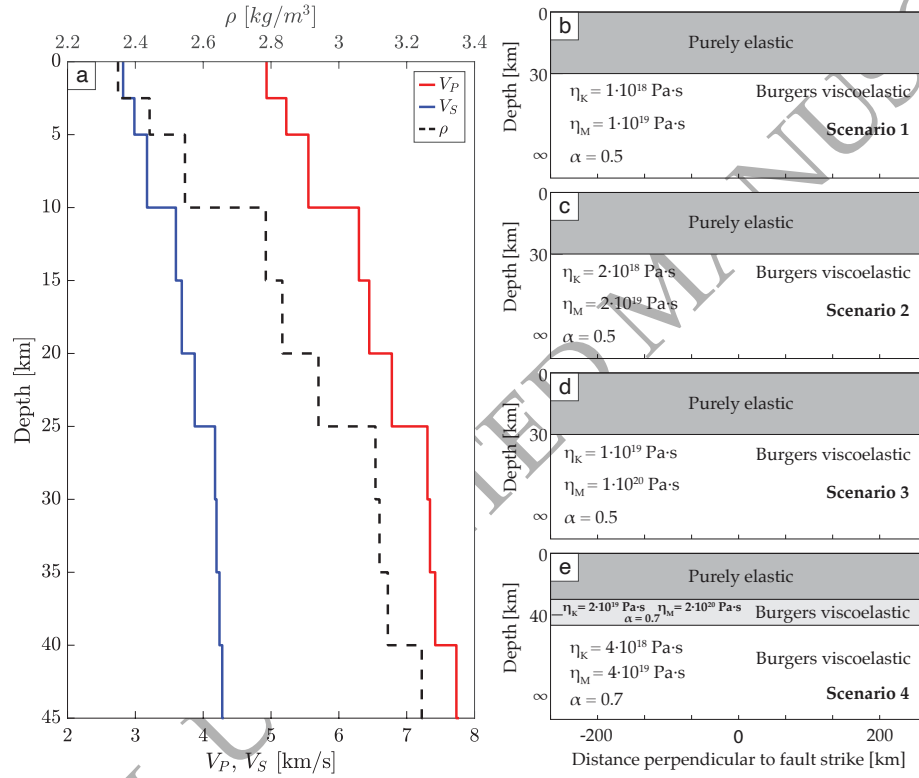


Figure 8: Panel a shows the simplified 1D layered Earth model of the Gulf of Aqaba (adapted from Tang et al. 2016). Panels b, c, d and e are schematic representation of the lithosphere for model scenarios 1, 2, 3 and 4, respectively. Viscoelastic parameters of the Kelvin and Maxwell elements are also given for each scenario: η_K is the transient viscosity (dashpot of the Kelvin solid), η_M represents the steady-state viscosity (dashpot of the Maxwell fluid). α corresponds to the ratio between effective and unrelaxed shear modulus $\frac{\mu_K}{\mu_K + \mu_M}$. The unrelaxed shear modulus (μ_M) can be derived from the values of S wave velocities (V_s) and densities (ρ) provided in panel a.

For each model scenario, we computed time series of postseismic displacements for the period spanning from the origin time of the 1995 Nuweiba earthquake to the year 2020. Postseismic velocities were then derived from the average displacement rate over the observation period of each GPS station. As can be seen in Fig. 9, model scenarios implementing lower transient and steady-state viscosities result in slightly higher postseismic rates compared with those including higher viscosities. The pattern of modelled postseismic velocities in all four cases is similar and shows left-lateral motion, which agrees with the coseismic slip prescribed in the finite-fault model. However, unlike the modelled interseismic velocities, the predicted postseismic deformation fields exhibit maximum fault-parallel velocities about 30 km away from the fault trace, with lower rates next to the fault and in the far-field.

To determine whether the back-slip model residuals shown in Fig. 7 can be explained by postseismic transient motions from the Nuweiba earthquake, we estimated the misfits resulting from subtracting modelled postseismic rates from the block model residuals. Fig. 10a depicts the misfit vectors obtained for the four postseismic model scenarios considered in our study. As done in the back-slip model, we discriminated between GPS stations located in the northern and southern regions adjacent to the gulf on the Arabian plate. The misfit distributions and RMS values for each postseismic model are shown in Fig. 10b-e.

Overall, the lowest RMS misfits east of the Aragonese fault were obtained by implementing model scenario 2 (green vectors in Fig. 10a). Modelled postseismic velocities in the north (east of Aragonese fault trace) lead to a reduction in the RMS misfit by $\sim 11\%$ and $\sim 1\%$ of the east and north velocity components, respectively. In contrast, the quality of the fit in the southern region of the gulf (east of the Arnona and Tiran fault traces) degraded by 4% and 41% in east and north velocity components, respectively. The reduction in the quality of the fit in this area is due to northwestward modelled postseismic velocities, which are not observed in the block-model residuals. As shown in Fig. 7, GPS-derived velocities are well-fit by the back-slip model in the gulf's southern region located

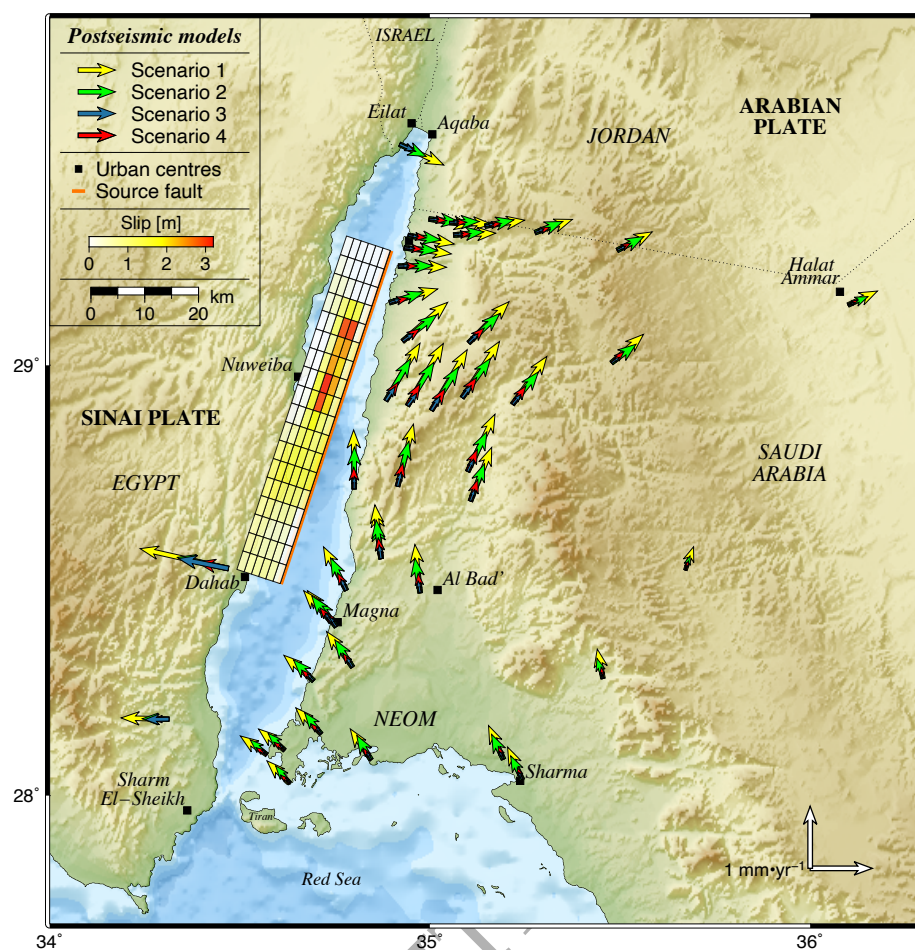


Figure 9: Modelled postseismic velocities computed at the location of GPS stations in the study area. Yellow, green, blue and red vectors represent modelled postseismic velocities for scenarios 1, 2, 3 and 4, respectively. Postseismic rates were estimated for the observation period at each GPS station (see Fig. S1 for details). The colour-coded grid represents the finite-source model of the Nuweiba earthquake derived by Baer et al. (2008). Note the change in velocity scale from previous figures.

east of the Arnona and Tiran faults. Hence, the consideration of any additional postseismic signal in the southern region of the gulf results in a degradation of the fit.

Our results suggest that modelled postseismic velocities induced by the 1995, $M_W 7.2$ Nuweiba earthquake explain part of the left-lateral residual motion observed in the lands bordering the gulf. However, the forward models fail to

satisfactorily reproduce the magnitudes of the residual velocity field by under-estimating somewhat the back-slip model residuals in the northeast of the gulf while overshooting observed residuals to the southeast.

7. Discussion

Previous estimates of the relative motion between the Sinai and Arabian plates along the Gulf of Aqaba relied on sparse observations at a limited number of GPS sites located on each side of the gulf (e.g., Mahmoud et al. 2005; Reilinger et al. 2006; ArRajehi et al. 2010; Gomez et al. 2020). However, the establishment of 27 survey-mode sites in 2014 and the rapid expansion of permanent geodetic networks in Saudi Arabia during the last decade have allowed us to derive an updated GPS velocity field of this region.

By implementing an elastic half-space model, we derived a slip rate of $4.9^{+0.9}_{-0.6}$ mm/yr and a locking depth of $6.8^{+3.5}_{-3.1}$ km across the Eilat fault. We also estimated a slip rate of $5.5^{+1.3}_{-0.9}$ mm/yr and a locking depth of $0.8^{+3.4}_{-0.8}$ km further south across the Arnona and Tiran faults (see red curves in Fig. 5a-b). While the slip rates derived here agree with previous studies, locking depth estimates are shallower than those reported along the Wadi Arabah fault north of the gulf, which range between 12 and 20 km (e.g., Le Beon et al. 2008; Sadeh et al. 2012; Masson et al. 2015; Hamiel et al. 2018b; Gomez et al. 2020). Further south, stations' rates show little evidence of strain accumulation despite their proximity to the Tiran fault. This pattern agrees with a very shallow locking depth, which might indicate potential creep along this fault segment (see Fig. 5b).

To evaluate the impact of outliers in the slip rate and locking depth inversions, we ran additional tests considering all the stations in the profiles including stations with anomalous rates. Inversions including all the GPS stations in the northern profile yielded a slip rate of $6.7^{+0.7}_{-0.7}$ mm/yr and a locking depth of $8.8^{+2.2}_{-2.2}$ km. Further south, across the Arnona and Tiran faults, this test resulted in a slip rate of $5.9^{+1.3}_{-0.7}$ mm/yr and a locking depth of $2.5^{+3.2}_{-2.2}$ km. Our results thus suggest that the slip rates seem to be more affected by the outlier

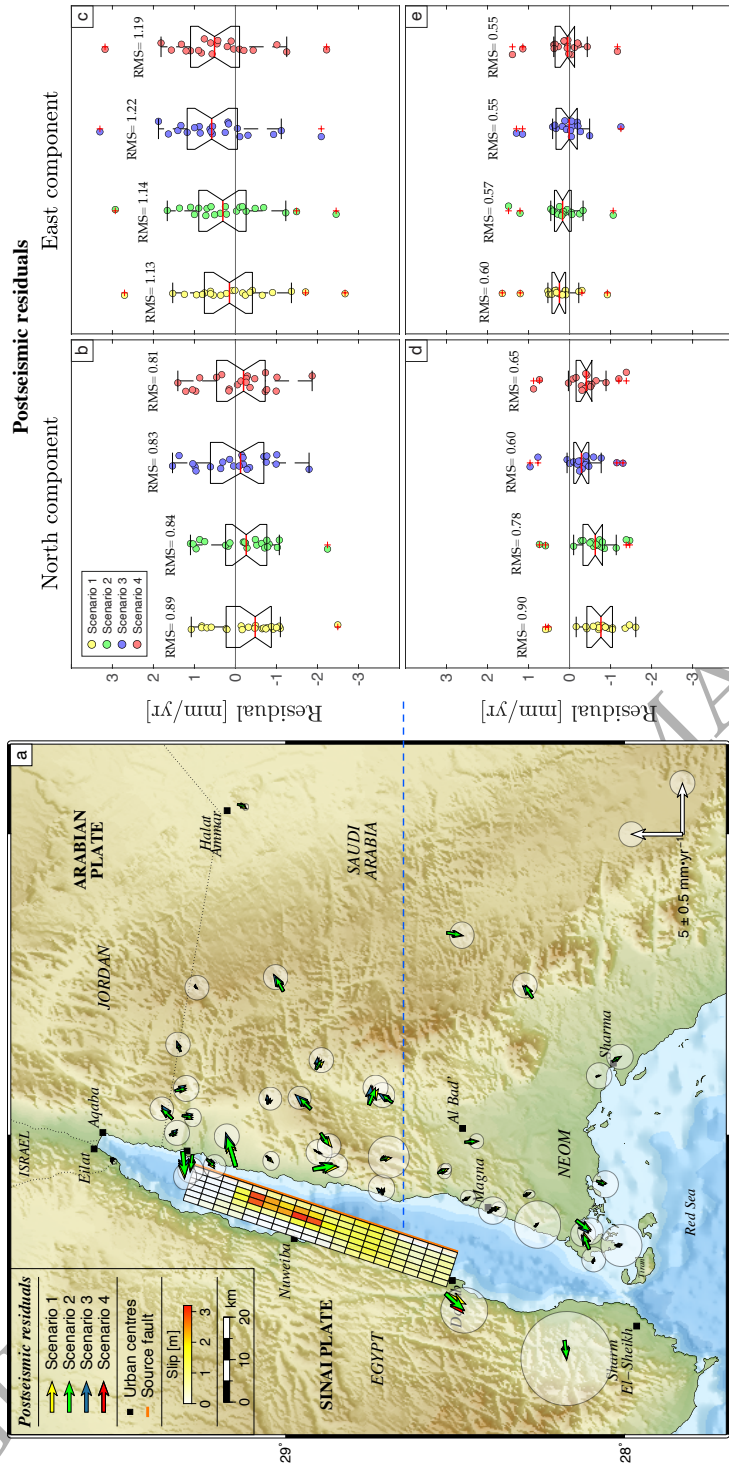


Figure 10: Residual velocities after implementing four postseismic model scenarios discussed in the text, with the orange line delineating the 1995 co-seismic fault rupture of the Aragonese fault (after Baer et al. 2008). For visualisation purpose, 95% confidence ellipses are shown only for the best fitting postseismic model (scenario 2). The contrast between the residuals of stations in the northern half of the gulf (East of the Aragonese fault trace) and South (East of the Armona fault trace) is illustrated in panels b-e, with notched boxes enclosing data within 25th and 75th percentiles. For each scenario, the median of the misfit distribution is shown as a solid red line and whiskers extend to the most extreme data points not considered as outliers, which are represented by the red crosses.

rates in the mid- and far-field than the locking depths (see Fig. S4). Although the slip rates and locking depths for the southern profile are not as well constrained as for the northern profile, our modelling results show that the buried screw dislocation model provides consistent locking depth estimates even in the presence of the outliers, indicating shallower locking depths in the south.

Previous geophysical studies conducted along the on-land portion of the DST and its offshore extension in the Gulf of Aqaba indicate a systematic thinning of the lithosphere towards the Red Sea (e.g., Ginzburg et al. 1979; Ben-Avraham 1985; Mohsen et al. 2006; El Khrepy et al. 2016a). Ben-Avraham (1985) conducted gravity, magnetic and seismic surveys in the gulf, and proposed a thinner crust in its southern region. This observation agrees with earlier investigations indicating higher heat flow values and gradual crustal thinning towards the south (e.g., Ginzburg et al. 1979; Ben-Avraham and Von Herzen 1987). Similarly, tomographic inversions and S-receiver function studies revealed that the lithospheric thickness decreases from 80 km north of the Dead Sea to 65 km in the Gulf of Aqaba, indicating stronger asthenospheric upwelling in the south (Mohsen et al., 2006; El Khrepy et al., 2016a). More recently, Li et al. (2021) implemented along-track Sentinel-1 burst-overlap interferometric time-series analysis and reported decreasing locking depths from 15.9 ± 1.9 km of the Wadi Arabah fault to only 3.9 ± 1.5 km in the southern part of the Gulf of Aqaba. Hence, the locking depth reduction from north to south along the Wadi Arabah and faults within the gulf might be explained by progressive crustal thinning towards the Red Sea.

We estimated a slip rate of ~ 4.5 mm/yr along the main fault segments in the gulf based on a forward back-slip model, which implemented the Arabia-Sinai Euler pole derived in this study. This estimate is lower than the best-fit inverted in our screw dislocation models, and could be attributed to potential internal deformation or fragmentation of the Sinai plate, as has been reported in recent studies (e.g., Gomez et al. 2020). The present-day slip rate derived from geodetic data in the gulf area agrees well with the long-term geological estimates along the southern on-land portion of the DST, which converge to an

average value of 5 ± 1 mm/yr (e.g., [Le Béon et al. 2010, 2012](#)). We can thus assume that the present-day slip rate has remained relatively constant over the last millennium. Based on this assumption, the Eilat and Arnona faults have accumulated significant moment since the last historical earthquakes that struck the gulf area in 1212 AD and 1588 AD (e.g., [Ambraseys 2009; Agnon 2014; Klinger et al. 2015; Lefevre et al. 2018](#)).

We estimated the slip deficit and moment accumulation rate on the major strike-slip faults in the gulf, assuming that they are fully locked during the interseismic period. We also considered an additional scenario assuming that the Tiran fault in the southern region of the gulf creeps aseismically. Considering that the 1212 AD and 1588 AD earthquakes cannot be unambiguously assigned to specific fault traces within the gulf, we tested both as potential last earthquakes on the Eilat and Arnona faults. For this purpose, we evaluated lower and upper bound estimates based on the fault kinematic parameters derived in this research and previous investigations along the southern on-land portion of the DST, corresponding to slip rates ranging between 4.4 and 5.2 mm/yr (e.g., [Mahmoud et al. 2005; Reilinger et al. 2006; Le Béon et al. 2008; ArRajehi et al. 2010; Al Tarazi et al. 2011; Sadeh et al. 2012; Masson et al. 2015; Hamiel et al. 2016, 2018a,b; Gomez et al. 2020](#)). For the locking depths, we considered the lower and upper bounds from the 1-sigma uncertainty derived in the gulf's northern region, corresponding to locking depths ranging between 4 and 10 km (see Fig. 5a).

Tab. 1 summarises the parameters considered in our calculations (fault length L , locking depth L_D , and slip rate \dot{u}) as well as estimates of the slip deficit u , geodetic moment M_0 , moment accumulation rate \dot{M}_0 and the associated moment magnitude M_W for each fault segment, which was computed based on the scaling regression by [Hanks and Kanamori \(1979\)](#). The slip deficit and moment accumulation rates estimated for the Eilat and Arnona faults suggest that impending earthquakes could reach M_W 6.7-7.3, assuming that the moment accumulated since the last known historical or instrumental earthquakes ("Last EQ") would be released by an earthquake on each fault strand. Estimates of the

slip deficit and moment accumulated on the Aragonese fault are much smaller, as expected, considering that this fault strand ruptured during the 1995 $M_W 7.2$ Nuweiba earthquake (Klinger et al., 1999; Shamir et al., 2003; Hofstetter, 2003; Baer et al., 2008; Ribot et al., 2021). Our results thus agree with previous studies suggesting that the Eilat and Arnona faults might be in a late stage of their current interseismic period (e.g., Hamiel et al. 2018b; Kanari et al. 2020; Ribot et al. 2021).

Table 1: Fault parameters and estimated earthquake potential for the main strike-slip fault segments in the Gulf of Aqaba.

Fault	L [km]	L_D [km]	\dot{u} [mm/yr]	Last EQ	u [m]	M_0 [Nm]	\dot{M}_0 [Nm/yr]	M_W
Eilat	59	4	4.4	1212	3.56	2.517×10^{19}	3.115×10^{16}	6.9
		10	5.2		4.20	7.437×10^{19}	9.204×10^{16}	7.2
	59	4	4.4	1588	1.90	1.346×10^{19}	3.115×10^{16}	6.7
		10	5.2		2.25	3.976×10^{19}	9.204×10^{16}	7.0
Aragonese	53	4	4.4	1995	0.11	6.996×10^{17}	2.798×10^{16}	5.9
		10	5.2		0.13	2.067×10^{18}	8.268×10^{16}	6.2
Arnona	83	4	4.4	1212	3.56	3.541×10^{19}	4.382×10^{16}	7.0
		10	5.2		4.20	1.046×10^{20}	1.295×10^{17}	7.3
	83	4	4.4	1588	1.90	1.893×10^{19}	4.382×10^{16}	6.8
		10	5.2		2.25	5.593×10^{19}	1.295×10^{17}	7.1
Tiran	50	Creep	4.4 5.2	-	-	-	-	-

Our modelling results reveal a residual left-lateral motion across the gulf that cannot be resolved by standard models of interseismic strain accumulation (Figs. 7 and 10). The nature of these velocity residuals is a subject of debate. While some studies speculate that they could be caused by interseismic elastic strain accumulation along the faults bounding the pull-apart basins in the Gulf of Aqaba (e.g., Pietrantonio et al. 2016), others point out that they could be due to postseismic motions induced by the 1995 Nuweiba Earthquake (e.g., Piersanti et al. 2001; Pe'eri et al. 2002; Riguzzi et al. 2006; Gomez et al. 2020).

We consider four possible explanations for the left-lateral residual motion observed across the gulf. The first possibility is that anomalous misfits are due to poor Euler vector parameters for the Sinai subplate relative to ITRF2014. However, this explanation is not supported by the velocity field obtained for stations of the GIL network in Israel, which exhibit residual velocities close to

zero, evidencing the robustness of the Euler vector parameters derived in our study (see Tab. S2 and Fig. S2). A second possibility is that the resulting misfits reflect the difference in temporal baselines between stations situated in the northern and southern regions of the gulf, as shown in Fig. S1. This hypothesis might explain the small residuals obtained for stations with longer time series located east of the Arnona fault (sites MAG1, MAG2 and BIDA, RASH, TAYS, TAY1, TB03, SHRM). Nevertheless, it fails to explain the systematic nature of residual motions.

A third hypothesis is that the relative motion between the Arabian and Sinai plates along the Gulf of Aqaba is accommodated by a wide deformation zone extending up to ~ 50 km across both plates. Several studies have identified two shear belts composed of anastomosing faults on both sides of the gulf (e.g., Freund et al. 1970; Bartov et al. 1980; Eyal et al. 1981; Garfunkel 1981; Lyberis 1988). Earlier investigations indicate that these faults were active primarily during the first slip stages along the DST and do not affect post-Miocene stratigraphic units (e.g., Bartov et al. 1980; Eyal et al. 1981; Garfunkel 1981). A more recent study reported small-scale normal faults affecting post-Miocene strata and Pleistocene coral terraces, indicating ENE-WSW extension (Bosworth et al., 2017). However, the seismicity recorded in the gulf area shows that most earthquakes concentrate along the gulf itself and the coastal plains (e.g., Ben-Avraham et al. 1979; Bartov et al. 1980, Fig. 2), suggesting that recent deformation is confined to those areas.

Finally, the systematic left-lateral residual signal could reflect ongoing post-seismic deformation caused by the Nuweiba Earthquake. A recent study by Liu et al. (2020) found that the lower crust exhibits ductility at decadal time scales, and thus postseismic transient motions may be larger and more enduring than previously thought. As noted by Piersanti et al. (2001), the motion of stations DAHA and NABQ on the Sinai side of the gulf is puzzling, considering that they exhibit motions that are opposite to the direction predicted by interseismic models of strain accumulation (see Fig. 3). Similarly, the updated velocity field presented in this study allowed us to quantitatively identify northeastward

residuals east of the Aragonese and Eilat faults, which agree with the overall pattern of modelled postseismic rates.

We speculate that the misfit between the magnitudes of theoretical postseismic motions and residuals from the back-slip model may arise from structural and rheological complexities in the gulf (e.g., [Ben-Avraham 1985](#); [El Khrepy et al. 2016a,b](#)), which were not considered in our forward models. Therefore, postseismic motions and relaxation times could exhibit significant spatial variations depending on the lithospheric structure in different regions of the gulf and the slip distribution used to model the Nuweiba earthquake.

8. Conclusions

The establishment of 27 survey-mode GPS stations in 2014 and the analysis of up to 19 years of geodetic observations on the Arabian and Sinai-Levant plates allowed us to derive an updated crustal motion velocity field of the lands bordering the Gulf of Aqaba. By implementing an elastic interseismic model, we derived a slip rate of $4.9^{+0.9}_{-0.6} \text{ mm/yr}$ and a locking depth of $6.8^{+3.5}_{-3.1} \text{ km}$ across the Eilat fault in the gulf's northern region. Our modelling results suggest that either a shallow locking depth or creeping might be required to explain the low interseismic strain accumulation observed in the gulf's southern region across Tiran fault. We identified a systematic left-lateral residual motion across the gulf, characterised by northeastward residuals east of the Aragonese fault and southwestward residuals west of the Arnona fault. We postulate that postseismic transient motions caused by the 1995, $M_W 7.2$ Nuweiba earthquake could potentially explain these misfits. Estimates of the geodetic moment accumulated on the Eilat and Arnona faults since the last historical earthquakes that struck the gulf area in 1212 AD and 1588 AD indicate that impending earthquakes on these faults could potentially reach $M_W 6.7-7.3$, posing a significant hazard to the urban centres along the gulf coast. Future studies would benefit from incorporating additional GPS stations on the Sinai side of the gulf, refined slip models of the Nuweiba earthquake and more detailed information about

historical earthquakes in the gulf region.

Acknowledgements

We thank Hannes Vasyura-Bathke, Joël Ruch, Jon Harrington, Samer Almashharawi, Mohammad Youssef, Laura Parisi, Adel Sherif and the students of the 2015 Seismotectonics course at KAUST for the help with the GPS fieldwork campaigns. We also thank the Saudi Geological Survey (SGS) and King Abdulaziz City for Science and Technology (KACST) for providing the continuous GPS data from the gulf's stations. Maps were generated using the Generic Mapping Tools, Version 5.4.5 (Wessel et al. 2013, <https://www.generic-mapping-tools.org>). This research was supported by King Abdullah University of Science and Technology (KAUST), under award number OSR-2016-CRG5-3027.

Data Availability

The GPS data underlying this article will be made available on the UNAVCO archive, at <https://www.unavco.org/data/dai/>.

Agnon A. Pre-instrumental earthquakes along the dead sea rift. In: Dead Sea transform fault system: reviews. Springer; 2014. p. 207–61.

Al Tarazi E, Abu Rajab J, Gomez F, Cochran W, Jaafar R, Ferry M. GPS measurements of near-field deformation along the southern Dead Sea Fault System: GPS along the southern Dead Sea Fault. *Geochemistry, Geophysics, Geosystems* 2011;12(12). doi:[10.1029/2011GC003736](https://doi.org/10.1029/2011GC003736).

Alamri AM, Schult ER, Bufe CG. Seismicity and aeromagnetic features of the Gulf of Aqaba (Elat) Region. *Journal of Geophysical Research: Solid Earth* 1991;96(B12):20179–85. doi:[10.1029/91JB02104](https://doi.org/10.1029/91JB02104).

Altamimi Z, Métivier L, Rebischung P, Rouby H, Collilieux X. ITRF2014 plate motion model. *Geophysical Journal International* 2017;209(3):1906–12. doi:[10.1093/gji/ggx136](https://doi.org/10.1093/gji/ggx136).

- Ambraseys N. Earthquakes in the Mediterranean and Middle East: a multidisciplinary study of seismicity up to 1900. Cambridge University Press, 2009.
- ArRajehi A, McClusky S, Reilinger R, Daoud M, Alchalbi A, Ergintav S, Gomez F, Sholan J, Bou-Rabee F, Ogubazghi G, Haileab B, Fisseha S, Asfaw L, Mahmoud S, Rayan A, Bendik R, Kogan L. Geodetic constraints on present-day motion of the Arabian Plate: Implications for Red Sea and Gulf of Aden rifting: Arabia plate motion. *Tectonics* 2010;29(3). doi:[10.1029/2009TC002482](https://doi.org/10.1029/2009TC002482).
- Baer G, Funning GJ, Shamir G, Wright TJ. The 1995 November 22, Mw 7.2 Gulf of Elat earthquake cycle revisited. *Geophysical Journal International* 2008;175(3):1040–54. doi:[10.1111/j.1365-246X.2008.03901.x](https://doi.org/10.1111/j.1365-246X.2008.03901.x).
- Bar M, Kolodny Y, Bentor Y. Dating faults by fission track dating of epidotes—an attempt. *Earth and Planetary Science Letters* 1974;22(2):157–62.
- Bartov Y, Steinitz G, Eyal M, Eyal Y. Sinistral movement along the Gulf of Aqaba — its age and relation to the opening of the Red Sea. *Nature* 1980;285:220. URL: <http://dx.doi.org/10.1038/285220a0>.
- Becker J, Sandwell D, Smith W, Braud J, Binder B, Depner J, Fabre D, Factor J, Ingalls S, Kim S, et al. Global bathymetry and elevation data at 30 arc seconds resolution: Srtm30_plus. *Marine Geodesy* 2009;32(4):355–71.
- Ben-Avraham Z. Structural framework of the Gulf of Elat (Aqaba), Northern Red Sea. *Journal of Geophysical Research: Solid Earth* 1985;90(B1):703–26. doi:[10.1029/JB090iB01p00703](https://doi.org/10.1029/JB090iB01p00703).
- Ben-Avraham Z, Almogor G, Garfunkel Z. Sediments and structure of the Gulf of Elat (Aqaba)—Northern Red Sea. *Sedimentary Geology* 1979;23(1-4):239–67. doi:[10.1016/0037-0738\(79\)90016-2](https://doi.org/10.1016/0037-0738(79)90016-2).
- Ben-Avraham Z, Lazar M, Garfunkel Z, Reshef M, Ginzburg A, Rotstein Y, Frieslander U, Bartov Y, Shulman H. Structural styles along the Dead Sea

- Fault. In: *Regional Geology and Tectonics: Phanerozoic Passive Margins, Cratonic Basins and Global Tectonic Maps*. Elsevier; 2012. p. 616–33. doi:[10.1016/B978-0-444-56357-6.00016-0](https://doi.org/10.1016/B978-0-444-56357-6.00016-0).
- Ben-Avraham Z, Von Herzen RP. Heat flow and continental breakup: the gulf of elat (aqaba). *Journal of Geophysical Research: Solid Earth* 1987;92(B2):1407–16.
- Ben-Avraham Z, Zoback MD. Transform-normal extension and asymmetric basins: An alternative to pull-apart models. *Geology* 1992;20(5):423–6.
- Bock Y, Wdowinski S, Fang P, Zhang J, Williams S, Johnson H, Behr J, Genrich J, Dean J, van Domselaar M, Agnew D, Wyatt F, Stark K, Oral B, Hudnut K, King R, Herring T, Dinardo S, Young W, Jackson D, Gurtner W. Southern california permanent gps geodetic array: Continuous measurements of regional crustal deformation between the 1992 landers and 1994 northridge earthquakes. *Journal of Geophysical Research: Solid Earth* 1997;102(B8):18013–33. doi:[10.1029/97JB01379](https://doi.org/10.1029/97JB01379).
- Bos MS, Fernandes RMS, Williams SDP, Bastos L. Fast error analysis of continuous gnss observations with missing data. *Journal of Geodesy* 2013;87(4):351–60. doi:[10.1007/s00190-012-0605-0](https://doi.org/10.1007/s00190-012-0605-0).
- Bosworth W, Montagna P, Pons-Branchu E, Rasul N, Taviani M. Seismic hazards implications of uplifted pleistocene coral terraces in the gulf of aqaba. *Scientific reports* 2017;7(1):1–13.
- Bürgmann R, Segall P, Lisowski M, Svarc J. Postseismic strain following the 1989 loma prieta earthquake from gps and leveling measurements. *Journal of Geophysical Research: Solid Earth* 1997;102(B3):4933–55.
- Dong D, Herring TA, King RW. Estimating regional deformation from a combination of space and terrestrial geodetic data. *Journal of Geodesy* 1998;72(4):200–14. doi:[10.1007/s001900050161](https://doi.org/10.1007/s001900050161).

- Dziewonski A, Chou TA, Woodhouse JH. Determination of earthquake source parameters from waveform data for studies of global and regional seismicity. *Journal of Geophysical Research: Solid Earth* 1981;86(B4):2825–52.
- Ekström G, Nettles M, Dziewoński A. The global cmt project 2004–2010: Centroid-moment tensors for 13,017 earthquakes. *Physics of the Earth and Planetary Interiors* 2012;200:1–9.
- El-Aal AEAKA, Badreldin H. Seismological aspects of the 27 june 2015 gulf of aqaba earthquake and its sequence of aftershocks. *Journal of Seismology* 2016;20(3):935–52.
- El-Isa ZH, Merghelani HM, Bazzari MA. The Gulf of Aqaba earthquake swarm of 1983 January–April. *Geophysical Journal International* 1984;78(3):711–22. doi:[10.1111/j.1365-246X.1984.tb05066.x](https://doi.org/10.1111/j.1365-246X.1984.tb05066.x).
- El Khrepy S, Koulakov I, Al-Arif N, Petrunin AG. Seismic structure beneath the Gulf of Aqaba and adjacent areas based on the tomographic inversion of regional earthquake data. *Universitätsbibliothek Johann Christian Senckenberg*, 2016a.
- El Khrepy S, Koulakov I, Al-Arifi N. Crustal and uppermost mantle structure beneath the continental rifting area of the gulf of suez from earthquake tomography. *Tectonophysics* 2016b;668:92–104.
- Elias A, Tapponnier P, Singh SC, King GC, Briaies A, Daëron M, Carton H, Sursock A, Jacques E, Jomaa R, Klinger Y. Active thrusting offshore Mount Lebanon: Source of the tsunamigenic A.D. 551 Beirut-Tripoli earthquake. *Geology* 2007;35(8):755–8. doi:[10.1130/G23631A.1](https://doi.org/10.1130/G23631A.1).
- Eyal M, Eyal Y, Bartov Y, Steinitz G. The tectonic development of the western margin of the Gulf of Elat (Aqaba) rift. *Tectonophysics* 1981;80(1-4):39–66. doi:[10.1016/0040-1951\(81\)90141-4](https://doi.org/10.1016/0040-1951(81)90141-4).
- Freed AM, Bürgmann R. Evidence of power-law flow in the mojave desert mantle. *Nature* 2004;430(6999):548.

- Freund R, Garfunkel Z, Zak I, Goldberg M, Weissbrod T, Derin B, Bender F, Wellings F, Girdler R. The shear along the dead sea rift. Philosophical Transactions for the Royal Society of London Series A, Mathematical and Physical Sciences 1970;:107–30.
- Garfunkel Z. Internal structure of the Dead Sea leaky transform (rift) in relation to plate kinematics. Tectonophysics 1981;80(1-4):81–108. doi:[10.1016/0040-1951\(81\)90143-8](https://doi.org/10.1016/0040-1951(81)90143-8).
- Ginzburg A, Makris J, Fuchs K, Prodehl C, Kaminski W, Amitai U. A seismic study of the crust and upper mantle of the jordan-dead sea rift and their transition toward the mediterranean sea. Journal of Geophysical Research: Solid Earth 1979;84(B4):1569–82.
- Gomez F, Cochran WJ, Yassminh R, Jaafar R, Reilinger R, Floyd M, King RW, Barazangi M. Fragmentation of the Sinai Plate indicated by spatial variation in present-day slip rate along the Dead Sea Fault System. Geophysical Journal International 2020;221(3):1913–40. doi:[10.1093/gji/ggaa095](https://doi.org/10.1093/gji/ggaa095).
- Gomez F, Karam G, Khawlie M, McClusky S, Vernant P, Reilinger R, Jaafar R, Tabet C, Khair K, Barazangi M. Global Positioning System measurements of strain accumulation and slip transfer through the restraining bend along the Dead Sea fault system in Lebanon. Geophysical Journal International 2007;168(3):1021–8. doi:[10.1111/j.1365-246X.2006.03328.x](https://doi.org/10.1111/j.1365-246X.2006.03328.x).
- Hamiel Y, Masson F, Piatibratova O, Mizrahi Y. Gps measurements of crustal deformation across the southern arava valley section of the dead sea fault and implications to regional seismic hazard assessment. Tectonophysics 2018a;724:171–8.
- Hamiel Y, Masson F, Piatibratova O, Mizrahi Y. GPS measurements of crustal deformation across the southern Arava Valley section of the Dead Sea Fault and implications to regional seismic hazard assessment. Tectonophysics 2018b;724-725:171–8. doi:[10.1016/j.tecto.2018.01.016](https://doi.org/10.1016/j.tecto.2018.01.016).

- Hamiel Y, Piatibratova O. Style and distribution of slip at the margin of a pull-apart structure: Geodetic investigation of the southern dead sea basin. *Journal of Geophysical Research: Solid Earth* 2019;124(11):12023–33.
- Hamiel Y, Piatibratova O, Mizrahi Y. Creep along the northern Jordan Valley section of the Dead Sea Fault. *Geophysical Research Letters* 2016;43(6):2494–501. doi:[10.1002/2016GL067913](https://doi.org/10.1002/2016GL067913).
- Hamiel Y, Piatibratova O, Mizrahi Y, Nahmias Y, Sagy A. Crustal Deformation across the Jericho Valley Section of the Dead Sea Fault as Resolved by Detailed Field and Geodetic Observations. *Geophysical Research Letters* 2018c;45(7):3043–50. doi:[10.1002/2018GL077547](https://doi.org/10.1002/2018GL077547).
- Hanks TC, Kanamori H. A moment magnitude scale. *Journal of Geophysical Research: Solid Earth* 1979;84(B5):2348–50. doi:[10.1029/JB084iB05p02348](https://doi.org/10.1029/JB084iB05p02348).
- Heimann A, Ron H. Young faults in the hula pull-apart basin, central dead sea transform. *Tectonophysics* 1987;141(1-3):117–24.
- Herring T, King R, McClusky S. Introduction to *gamt/gloabk*, release 10.7. Massachusetts Institute of Technology, Cambridge, Massachusetts 2018;.
- Hofstetter A. Seismic observations of the 22/11/1995 Gulf of Aqaba earthquake sequence. *Tectonophysics* 2003;369(1-2):21–36. doi:[10.1016/S0040-1951\(03\)00129-X](https://doi.org/10.1016/S0040-1951(03)00129-X).
- Hofstetter A, Dorbath C, Dorbath L. Instrumental data on the seismic activity along the dead sea transform. In: *Dead Sea Transform Fault System: Reviews*. Springer; 2014. p. 263–78. doi:[10.1007/978-94-017-8872-4_9](https://doi.org/10.1007/978-94-017-8872-4_9).
- Joffe S, Garfunkel Z. Plate kinematics of the circum Red Sea—a re-evaluation. *Tectonophysics* 1987;141(1-3):5–22. doi:[10.1016/0040-1951\(87\)90171-5](https://doi.org/10.1016/0040-1951(87)90171-5).
- Jónsson S. Importance of post-seismic viscous relaxation in southern iceland. *Nature Geoscience* 2008;1(2):136–9.

- Jónsson S, Segall P, Pedersen R, Björnsson G. Post-earthquake ground movements correlated to pore-pressure transients. *Nature* 2003;424(6945):179.
- Kagan E, Stein M, Agnon A, Neumann F. Intrabasin paleoearthquake and quiescence correlation of the late holocene dead sea. *Journal of Geophysical Research: Solid Earth* (1978–2012) 2011;116(B4). URL: <https://doi.org/10.1029/2010JB007452>. doi:10.1029/2010JB007452.
- Kanari M, Niemi TM, Ben-Avraham Z, Frieslander U, Tibor G, Goodman-Tchernov BN, Wechsler N, Abueladas A, Al-Zoubi A, Basson U, et al. Seismic potential of the dead sea fault in the northern gulf of aqaba-elat: New evidence from liquefaction, seismic reflection, and paleoseismic data. *Tectonophysics* 2020;793:228596.
- Klinger Y, Le Béon M, Al-Qaryouti M. 5000 yr of paleoseismicity along the southern dead sea fault. *Geophysical Journal International* 2015;202(1):313–27.
- Klinger Y, Rivera L, Haessler H. Active Faulting in the Gulf of Aqaba: New Knowledge from the Mw 7.3 Earthquake of 22 November 1995. *Bulletin of the Seismological Society of America* 1999;89(4):1025–36.
- Le Béon M, Klinger Y, Al-Qaryouti M, Mériaux AS, Finkel RC, Elias A, Mayyas O, Ryerson FJ, Tapponnier P. Early holocene and late pleistocene slip rates of the southern dead sea fault determined from 10be cosmogenic dating of offset alluvial deposits. *Journal of Geophysical Research: Solid Earth* 2010;115(B11).
- Le Béon M, Klinger Y, Amrat AQ, Agnon A, Dorbath L, Baer G, Ruegg JC, Charade O, Mayyas O. Slip rate and locking depth from GPS profiles across the southern Dead Sea Transform. *Journal of Geophysical Research* 2008;113(B11). doi:10.1029/2007JB005280.
- Le Béon M, Klinger Y, Mériaux AS, Al-Qaryouti M, Finkel RC, Mayyas O, Tapponnier P. Quaternary morphotectonic mapping of the wadi araba and

implications for the tectonic activity of the southern dead sea fault. *Tectonics* 2012;31(5).

Lefevre M, Klinger Y, Al-Qaryouti M, Le Béon M, Moumani K. Slip deficit and temporal clustering along the Dead Sea fault from paleoseismological investigations. *Scientific Reports* 2018;8(1). doi:[10.1038/s41598-018-22627-9](https://doi.org/10.1038/s41598-018-22627-9).

Li X, Jónsson S, Cao Y. Interseismic deformation from sentinel-1 burst-overlap interferometry: Application to the southern Dead Sea fault. *Geophysical Research Letters* 2021;doi:[10.1029/2021GL093481](https://doi.org/10.1029/2021GL093481).

Lisowski M, Savage JC, Prescott WH. The velocity field along the san andreas fault in central and southern california. *Journal of Geophysical Research: Solid Earth* 1991;96(B5):8369–89. doi:[10.1029/91JB00199](https://doi.org/10.1029/91JB00199).

Liu S, Shen ZK, Bürgmann R, Jónsson S. Thin crème brûlée rheological structure for the Eastern California Shear Zone. *Geology* 2020;doi:[10.1130/G47729.1](https://doi.org/10.1130/G47729.1).

Lyberis N. Tectonic evolution of the Gulf of Suez and the Gulf of Aqaba. *Tectonophysics* 1988;153(1-4):209–20. doi:[10.1016/0040-1951\(88\)90016-9](https://doi.org/10.1016/0040-1951(88)90016-9).

Mahmoud S, Reilinger R, McClusky S, Vernant P, Tealeb A. GPS evidence for northward motion of the Sinai Block: Implications for E. Mediterranean tectonics. *Earth and Planetary Science Letters* 2005;238(1-2):217–24. doi:[10.1016/j.epsl.2005.06.063](https://doi.org/10.1016/j.epsl.2005.06.063).

Mahmoud Y, Masson F, Meghraoui M, Cakir Z, Alchalbi A, Yavasoglu H, Yönlü O, Daoud M, Ergintav S, Inan S. Kinematic study at the junction of the East Anatolian fault and the Dead Sea fault from GPS measurements. *Journal of Geodynamics* 2013;67:30–9. doi:[10.1016/j.jog.2012.05.006](https://doi.org/10.1016/j.jog.2012.05.006).

Masson F, Hamiel Y, Agnon A, Klinger Y, Deprez A. Variable behavior of the Dead Sea Fault along the southern Arava segment from GPS measurements. *Comptes Rendus Geoscience* 2015;347(4):161–9. doi:[10.1016/j.crte.2014.11.001](https://doi.org/10.1016/j.crte.2014.11.001).

- McCaffrey R. Block kinematics of the pacific–north america plate boundary in the southwestern united states from inversion of gps, seismological, and geologic data. *Journal of Geophysical Research: Solid Earth* 2005;110(B7). doi:[10.1029/2004JB003307](https://doi.org/10.1029/2004JB003307).
- McCaffrey R. Time-dependent inversion of three-component continuous gps for steady and transient sources in northern cascadia. *Geophysical Research Letters* 2009;36(7). doi:[10.1029/2008GL036784](https://doi.org/10.1029/2008GL036784).
- McClusky S, Reilinger R, Mahmoud S, Ben Sari D, Tealeb A. GPS constraints on Africa (Nubia) and Arabia plate motions. *Geophysical Journal International* 2003;155(1):126–38. doi:[10.1046/j.1365-246X.2003.02023.x](https://doi.org/10.1046/j.1365-246X.2003.02023.x).
- McKenzie D. Active tectonics of the mediterranean region. *Geophysical Journal International* 1972;30(2):109–85.
- McKenzie D, Davies D, Molnar P. Plate tectonics of the red sea and east africa. *Nature* 1970;226(5242):243.
- Meade BJ, Hager BH. Block models of crustal motion in southern california constrained by gps measurements. *Journal of Geophysical Research: Solid Earth* 2005;110(B3). doi:[10.1029/2004JB003209](https://doi.org/10.1029/2004JB003209).
- Meghraoui M. Paleoseismic History of the Dead Sea Fault Zone. In: Beer M., Kougioumtzoglou L., Patelli E., Au IK. (eds). *Encyclopedia of Earthquake Engineering*; Springer Berlin Heidelberg, 2015. doi:[10.1007/978-3-642-36197-5_40-1](https://doi.org/10.1007/978-3-642-36197-5_40-1).
- Mohsen A, Kind R, Sobolev SV, Weber M, Group D. Thickness of the lithosphere east of the dead sea transform. *Geophysical Journal International* 2006;167(2):845–52.
- Nuriel P, Weinberger R, Kylander-Clark A, Hacker B, Craddock J. The onset of the Dead Sea transform based on calcite age-strain analyses. *Geology* 2017;45(7):587–90. doi:[10.1130/G38903.1](https://doi.org/10.1130/G38903.1).

- Okada Y. Surface deformation due to shear and tensile faults in a half-space. *Bulletin of the Seismological Society of America* 1985;75(4):1135–54.
- Pe’eri S, Wdowinski S, Shtibelman A, Bechor N, Bock Y, Nikolaidis R, van Domselaar M. Current plate motion across the Dead Sea Fault from three years of continuous GPS monitoring. *Geophysical Research Letters* 2002;29(14):42–1. doi:[10.1029/2001GL013879](https://doi.org/10.1029/2001GL013879).
- Peltzer G, Rosen P, Rogez F, Hudnut K. Postseismic rebound in fault step-overs caused by pore fluid flow. *Science* 1996;273(5279):1202–4.
- Piersanti A, Nostro C, Riguzzi F. Active displacement field in the suez-sinai area: the role of postseismic deformation. *Earth and Planetary Science Letters* 2001;193(1):13 – 23. doi:[https://doi.org/10.1016/S0012-821X\(01\)00485-X](https://doi.org/10.1016/S0012-821X(01)00485-X).
- Pietrantonio G, Devoti R, Mahmoud S, Riguzzi F. Kinematics of the Suez-Sinai area from combined GPS velocity field. *Journal of Geodynamics* 2016;102:231–8. doi:[10.1016/j.jog.2016.10.003](https://doi.org/10.1016/j.jog.2016.10.003).
- Pinar A, Türkelli N. Source inversion of the 1993 and 1995 Gulf of Aqaba earthquakes. *Tectonophysics* 1997;283(1-4):279–88. doi:[10.1016/S0040-1951\(97\)00070-X](https://doi.org/10.1016/S0040-1951(97)00070-X).
- Pollitz FF. Gravitational viscoelastic postseismic relaxation on a layered spherical earth. *Journal of Geophysical Research: Solid Earth* 1997;102(B8):17921–41.
- Quennell AM. The structural and geomorphic evolution of the dead sea rift. *Quarterly Journal of the Geological Society* 1958;114(1-4):1–24.
- Quennell AM. Tectonics of the dead sea rift. In: *Proceedings of the 20th international geological congress, Mexico*. volume 385; 1959. p. 403.
- Reilinger R, McClusky S, Vernant P, Lawrence S, Ergintav S, Cakmak R, Ozener H, Kadirov F, Guliev I, Stepanyan R, Nadariya M, Hahubia G, Mah-

- moud S, Sakr K, ArRajehi A, Paradissis D, Al-Aydrus A, Prilepin M, Guseva T, Evren E, Dmitrotsa A, Filikov SV, Gomez F, Al-Ghazzi R, Karam G. Gps constraints on continental deformation in the africa-arabia-urasia continental collision zone and implications for the dynamics of plate interactions. *Journal of Geophysical Research: Solid Earth* 2006;111(B5). doi:[10.1029/2005JB004051](https://doi.org/10.1029/2005JB004051).
- Ribot M, Klinger Y, Jónsson S, Avsar U, Pons-Branchu E, Matrau R, Mallon FL. Active faults' geometry in the gulf of aqaba, southern dead sea fault, illuminated by multibeam bathymetric data. *Tectonics* 2021;40(4). doi:<https://doi.org/10.1029/2020TC006443>.
- Riguzzi F, Pietrantonio G, Piersanti A, Mahmoud SM. Current motion and short-term deformations in the suex-sinai area from gps observations. *Journal of Geodynamics* 2006;41(5):485–99. doi:<https://doi.org/10.1016/j.jog.2006.01.006>.
- Sadeh M, Hamiel Y, Ziv A, Bock Y, Fang P, Wdowinski S. Crustal deformation along the dead sea transform and the carmel fault inferred from 12 years of gps measurements. *Journal of Geophysical Research: Solid Earth* 2012;117(B8). doi:[10.1029/2012JB009241](https://doi.org/10.1029/2012JB009241).
- Savage J, Lisowski M, Svarc J. Postseismic deformation following the 1989 (m=7.1) loma prieta, california, earthquake. *Journal of Geophysical Research: Solid Earth* 1994;99(B7):13757–65.
- Savage JC, Burford RO. Geodetic determination of relative plate motion in central California. *Journal of Geophysical Research* 1973;78(5):832–45. doi:[10.1029/JB078i005p00832](https://doi.org/10.1029/JB078i005p00832).
- Scholz CH. Earthquake prediction and hazard analysis. In *The Mechanics of Earthquakes and Faulting.*; Cambridge University Press. 2nd ed.; p. 351–414. doi:[10.1017/CB09780511818516.009](https://doi.org/10.1017/CB09780511818516.009).

- Shamir G, Baer G, Hofstetter A. Three-dimensional elastic earthquake modelling based on integrated seismological and InSAR data: the $M_w = 7.2$ Nuweiba earthquake, gulf of Elat/Aqaba 1995 November. *Geophysical Journal International* 2003;154(3):731–44. doi:[10.1046/j.1365-246X.2003.01978.x](https://doi.org/10.1046/j.1365-246X.2003.01978.x).
- Smith-Konter BR, Sandwell DT, Shearer P. Locking depths estimated from geodesy and seismology along the san andreas fault system: Implications for seismic moment release. *Journal of Geophysical Research: Solid Earth* 2011;116(B6). doi:[10.1029/2010JB008117](https://doi.org/10.1029/2010JB008117).
- Steinitz G, Bartov Y, Hunziker J. K-ar age determinations of some miocene–pliocene basalts in israel: their significance to the tectonics of the rift valley. *Geological Magazine* 1978;115(5):329–40.
- Tang Z, Julià J, Zahran H, Mai PM. The lithospheric shear-wave velocity structure of saudi arabia: Young volcanism in an old shield. *Tectonophysics* 2016;680:8 – 27. doi:<https://doi.org/10.1016/j.tecto.2016.05.004>.
- Thomas R, Parker ST, Niemi TM. Structural damage from earthquakes in the second–ninth centuries at the archaeological site of aila in aqaba, jordan. *bulletin of the American schools of oriental research* 2007;346(1):59–77.
- Vergnolle M, Pollitz F, Calais E. Constraints on the viscosity of the continental crust and mantle from gps measurements and postseismic deformation models in western mongolia. *Journal of Geophysical Research: Solid Earth* 2003;108(B10).
- Wang R, Lorenzo-Martín F, Roth F. PSGRN/PSCMP—a new code for calculating co-and post-seismic deformation, geoid and gravity changes based on the viscoelastic-gravitational dislocation theory. *Computers & Geosciences* 2006;32(4):527–41.
- Wdowinski S, Bock Y, Baer G, Prawirodirdjo L, Bechor N, Naaman S, Knafo R, Forrai Y, Melzer Y. Gps measurements of current crustal movements along the

dead sea fault. *Journal of Geophysical Research: Solid Earth* 2004;109(B5).
doi:[10.1029/2003JB002640](https://doi.org/10.1029/2003JB002640).

Wdowinski S, Bock Y, Forrai Y, Melzer Y, Baer G. The GIL network of continuous GPS monitoring in Israel for geodetic and geophysical applications. *Israel Journal of Earth Sciences* 2001;50(1):39–48. doi:[10.1560/TGPB-FLBG-XJW9-K2QY](https://doi.org/10.1560/TGPB-FLBG-XJW9-K2QY).

Weertman J, Weertman J. Elementary dislocation theory. Macmillan series in materials science. Macmillan, 1964.

Wessel P, Smith WH, Scharroo R, Luis J, Wobbe F. Generic mapping tools: improved version released. *Eos, Transactions American Geophysical Union* 2013;94(45):409–10.

Wright T, Parsons B, Fielding E. Measurement of interseismic strain accumulation across the north anatolian fault by satellite radar interferometry. *Geophysical Research Letters* 2001;28(10):2117–20. doi:[10.1029/2000GL012850](https://doi.org/10.1029/2000GL012850).

Zilberman E, Amit R, Porat N, Enzel Y, Avner U. Surface ruptures induced by the devastating 1068 ad earthquake in the southern arava valley, dead sea rift, israel. *Tectonophysics* 2005;408(1-4):79–99.